



**HAL**  
open science

## Kinematics of fault-related folding derived from a sandbox experiment

Sylvain Bernard, Jean-Philippe Avouac, Stéphane Dominguez, Martine Simoes

► **To cite this version:**

Sylvain Bernard, Jean-Philippe Avouac, Stéphane Dominguez, Martine Simoes. Kinematics of fault-related folding derived from a sandbox experiment. *Journal of Geophysical Research*, 2007, 112 (B3), pp.B03S12. 10.1029/2005JB004149 . hal-02158007

**HAL Id: hal-02158007**

**<https://hal.science/hal-02158007>**

Submitted on 30 Jul 2020

**HAL** is a multi-disciplinary open access archive for the deposit and dissemination of scientific research documents, whether they are published or not. The documents may come from teaching and research institutions in France or abroad, or from public or private research centers.

L'archive ouverte pluridisciplinaire **HAL**, est destinée au dépôt et à la diffusion de documents scientifiques de niveau recherche, publiés ou non, émanant des établissements d'enseignement et de recherche français ou étrangers, des laboratoires publics ou privés.

## Kinematics of fault-related folding derived from a sandbox experiment

Sylvain Bernard,<sup>1,2</sup> Jean-Philippe Avouac,<sup>1</sup> Stéphane Dominguez,<sup>3</sup> and Martine Simoes<sup>1,4</sup>

Received 8 November 2005; revised 14 September 2006; accepted 6 October 2006; published 17 February 2007.

[1] We analyze the kinematics of fault tip folding at the front of a fold-and-thrust wedge using a sandbox experiment. The analog model consists of sand layers intercalated with low-friction glass bead layers, deposited in a glass-sided experimental device and with a total thickness  $h = 4.8$  cm. A computerized mobile backstop induces progressive horizontal shortening of the sand layers and therefore thrust fault propagation. Active deformation at the tip of the forward propagating basal décollement is monitored along the cross section with a high-resolution CCD camera, and the displacement field between pairs of images is measured from the optical flow technique. In the early stage, when cumulative shortening is less than about  $h/10$ , slip along the décollement tapers gradually to zero and the displacement gradient is absorbed by distributed deformation of the overlying medium. In this stage of detachment tip folding, horizontal displacements decrease linearly with distance toward the foreland. Vertical displacements reflect a nearly symmetrical mode of folding, with displacements varying linearly between relatively well defined axial surfaces. When the cumulative slip on the décollement exceeds about  $h/10$ , deformation tends to localize on a few discrete shear bands at the front of the system, until shortening exceeds  $h/8$  and deformation gets fully localized on a single emergent frontal ramp. The fault geometry subsequently evolves to a sigmoid shape and the hanging wall deforms by simple shear as it overthrusts the flat ramp system. As long as strain localization is not fully established, the sand layers experience a combination of thickening and horizontal shortening, which induces gradual limb rotation. The observed kinematics can be reduced to simple analytical expressions that can be used to restore fault tip folds, relate finite deformation to incremental folding, and derive shortening rates from deformed geomorphic markers or growth strata.

**Citation:** Bernard, S., J.-P. Avouac, S. Dominguez, and M. Simoes (2007), Kinematics of fault-related folding derived from a sandbox experiment, *J. Geophys. Res.*, 112, B03S12, doi:10.1029/2005JB004149.

### 1. Introduction

[2] Abandoned fluvial or alluvial terraces, as well as growth strata, can be used to determine incremental deformation associated with active folds [e.g., *Rockwell et al.*, 1988; *Suppe et al.*, 1992; *Hardy and Poblet*, 1994; *Molnar et al.*, 1994; *Hardy et al.*, 1996; *Storti and Poblet*, 1997; *Lavé and Avouac*, 2000; *Van der Woerd et al.*, 2001; *Thompson et al.*, 2002; *Simoes et al.*, 2007a]. If a unit can be traced all the way across a given fold, it can be used to estimate uplift since its deposition, and then to derive the corresponding average shortening from a mass balance calculation [*Chamberlin*, 1910; *Epard and Groshong*, 1993] (Figure 1). Although this geometrical approach can

be used to estimate cumulative shortening, it can only rarely be applied to geomorphic markers since a terrace record is often discontinuous and buried below younger sediments in the foreland or in piggyback basins. An alternative approach consists in fitting the terrace record from a model of folding constrained from pregrowth strata (structural measurements or subsurface data). This approach has been applied to fault bend folds (Figure 2a) assuming that the hanging wall deforms by flexural slip folding [*Lavé and Avouac*, 2000; *Thompson et al.*, 2002]. In such a case, where both bed length and thickness are constant, the local uplift  $U$  relative to the footwall, assumed rigid, obeys

$$U(x) = i(x) + b = R(z) \sin \theta(x), \quad (1)$$

where  $x$  is the distance along the section line,  $i(x)$  is the river incision since terrace abandonment,  $b$  is the base level change since terrace abandonment (positive upward),  $\theta(x)$  is the local bedding dip angle, and  $R(z)$  is the horizontal shortening since terrace abandonment of the layer at elevation  $z$ , which crops out at distance  $x$  from the trailing edge of the section (Figure 1). Base level change may lead to either entrenchment ( $b < 0$ ) or aggradation ( $b > 0$ ) in the foreland. On the sketch in Figure 1, we have assumed no

<sup>1</sup>Tectonics Observatory, California Institute of Technology, Pasadena, California, USA.

<sup>2</sup>Now at Laboratoire de Géologie, CNRS, Ecole Normale Supérieure, Paris, France.

<sup>3</sup>Laboratoire Dynamique de la Lithosphère, CNRS, Université Montpellier 2, Montpellier, France.

<sup>4</sup>Now at Géosciences Rennes, CNRS, Université Rennes 1, Rennes, France.

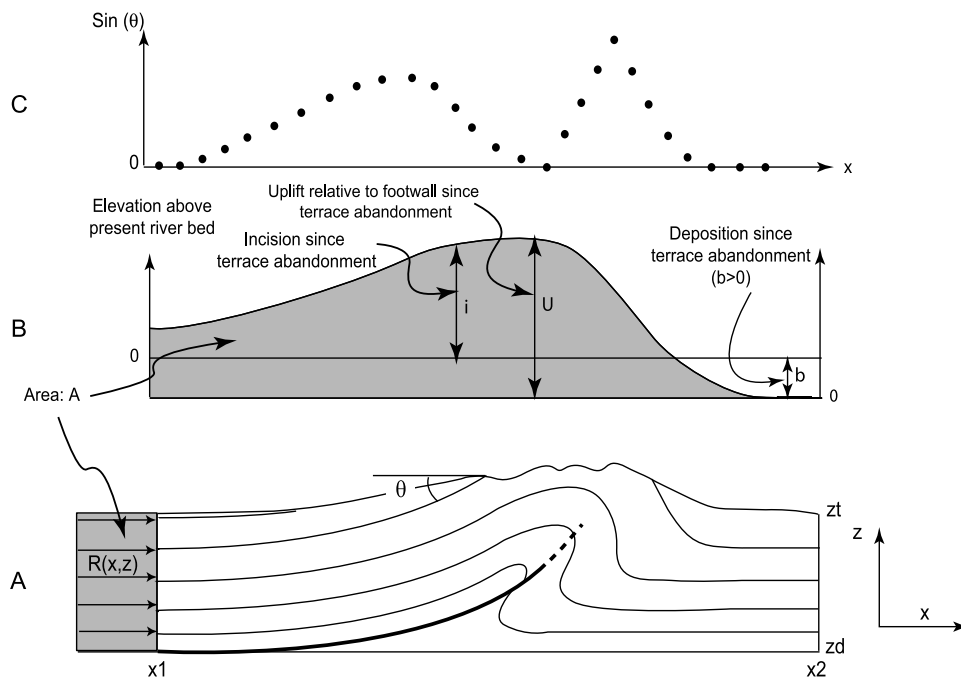


**Figure 1.** (a) Structure of a mature fault tip fold. (b) Continuous profile of a deformed terrace across the fold can be used to measure incremental folding. The area  $A$  defined by the deformed terrace above its initial geometry can be related to the total displaced area at the back of the fold since the terrace was abandoned. (c) Sine of bedding dip angle along structural section, as for use in equation (1). It is appropriate to perform such analysis to retrieve incremental deformation within the back limb of the fault tip fold represented, since it appears to be more mature in this portion of the fold, but this may lead to large errors at the front where the structure is not mature enough and appears more complex.

bed-parallel shear away from the fault zone; hence  $R$  is independent of  $z$ . In that case, estimating  $R$  does not require a continuous terrace profile and it is sufficient to use only a few independent estimates of the entrenchment rate at places with different dip angles in the zone where the bedding is already parallel to the fault plane (i.e., back limb of the fold represented in Figure 1). In principle, from estimates of incision rate, two points at least with different dip angles are necessary to derive both  $R$  and  $b$  [Thompson *et al.*, 2002]. When sufficiently complete terrace records are available, the relationship expressed by (1) is testable since it predicts that uplift and the sinus of the local bedding dip angle,  $\sin(\theta)$ , are proportional. Irrespective of the geomorphic record, it is important to note that this approach does not apply all along the profile of the fold, but only where the bedding is parallel to the fault plane (Figures 1 and 2).

[3] Fault tip folds can develop by distributed pure shear, with requisite bed length and thickness changes associated with limb rotation [Dahlstrom, 1990; Erslev, 1991; Poblet and McClay, 1996; Mitra, 2003], or by kink band migration and bed-parallel simple shear as in the case of fault propagation folds [Suppe and Medwedeff, 1990; Mosar and Suppe, 1992]. In either case, beds near the surface are not everywhere parallel to the thrust fault at depth, so that equation (1) does not hold in places like the fold forelimb in Figure 1. Figure 2b shows a number of acceptable kinematic models of fault tip folds, all based on the assumption of mass conservation. Most of these models are commonly

used to guide interpretation of structural measurements or seismic profiles [Erslev, 1991; Mosar and Suppe, 1992; Wickham, 1995; Storti and Poblet, 1997; Allmendinger, 1998; Allmendinger and Shaw, 2000; Brooks *et al.*, 2000; Zehnder and Allmendinger, 2000; Mitra, 2003]. In contrast to these purely geometric models, some authors have explored the possibility of modeling folds from the theory of elastic dislocations in an elastic half-space [Myers and Hamilton, 1964; King *et al.*, 1988; Stein *et al.*, 1988; Ward and Valensise, 1994; Savage and Cooke, 2004]. Although these various fold models might be used to analyze growth strata or deformed alluvial terraces and retrieve the kinematic history of folding, two difficulties generally arise. One is that the choice of a kinematic model is not straightforward, even when the geometry of growth strata is well constrained. The other is that the mathematical implementation of these models and the adjustment to field data are generally not simple. For these reasons, we seek a simple alternative relationship linking local uplift and/or bedding tilt to structural geometry. This relationship must be applicable across an entire structure and must be grounded in realistic fold kinematics or mechanics. For this purpose, we analyze folding produced in an analogue experiment to derive some simple kinematic model.

[4] It has been observed that the formation of the most frontal ramp in analogue models of wedge mechanics is preceded by a phase of distributed deformation which resembles fault tip folding [Dominguez *et al.*, 2001]. We therefore focused the present study on this particular phase,

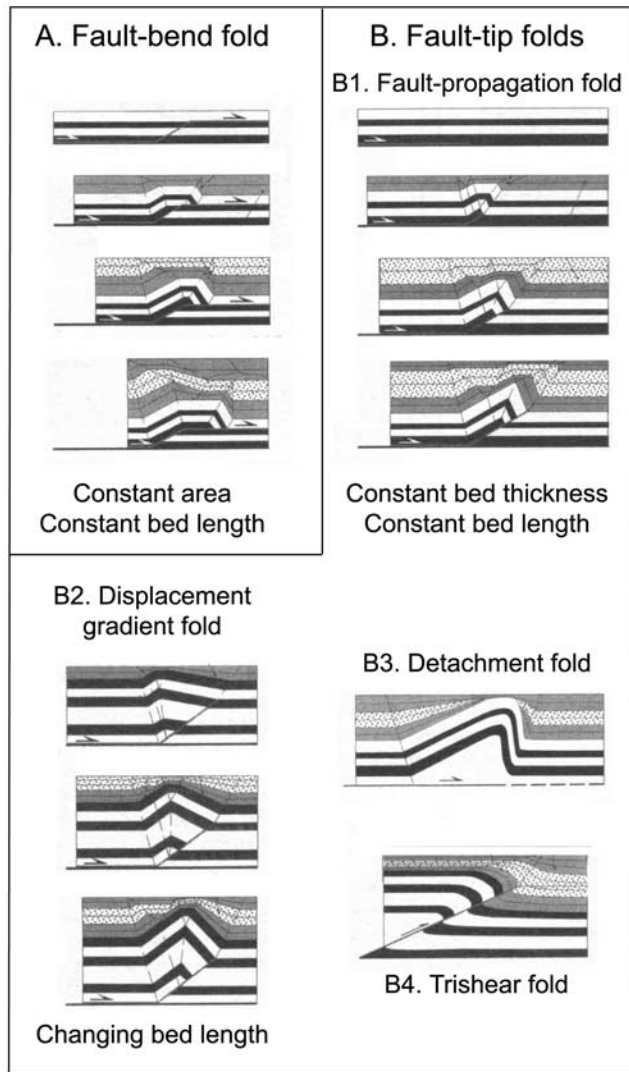


**Figure 2.** Classification of fold models with emphasis on the kinematic record provided by the architecture of growth strata [Burbank and Anderson, 2001]. (a) Fault bend folding [Suppe, 1983; Medwedeff and Suppe, 1997] results from the transfer of slip from a deeper to a shallower stratigraphic detachment level. The model assumes conservation of bed thickness and length during deformation. The hanging wall deforms by bed-parallel simple shear and axial surface migration. This model applies to mature faults, with a cumulative slip larger than the distance from the décollement to the surface (measured along the fault). (b) Various possible geometries of folds formed at the tip of a blind thrust fault. The fault propagation fold model (B1) assumes conservation of bed length and thickness [Suppe and Medwedeff, 1990; Mosar and Suppe, 1992]. The slip gradient model (B2) does not require fault propagation. It assumes conservation of area but not of bed length [Wickham, 1995]. Model B3 assumes a changing bed length and forelimb angle [Dahlstrom, 1990; Epard and Groshong, 1995; Mitra, 2003]. Model B4 assumes a triangular shaped zone of distributed shear [Erslev, 1991; Allmendinger, 1998]. The choice of the appropriate model to use in the analysis of a natural case example is non trivial.

assuming it can be considered to simulate the kinematics of the early stage of fault-related folding at the natural scale. With this aim, we used a new experimental setup that allows accurate measurements of fault slip kinematics and of the associated deformation field [Dominguez et al., 2003].

[5] We first present the experimental setup and the principles of the approach. We then describe in detail the evolution of incremental deformation during a representative experiment selected among more than 10 performed experiments, and derive some simple analytical approximations. Finally, we propose and test a procedure that can be used to restore incremental or cumulative deformation across fault tip folds. All variables introduced in the analysis are listed and defined in Table 1.

## 2. Experimental Setup

[6] The physical properties of dry sand and glass beads ( $\phi_s \sim 30^\circ$ , low-cohesion, time-independent mechanical behavior) make them good analogue materials to simulate brittle deformation of the upper crust at the laboratory scale [e.g., Malavieille, 1984; Mulugeta, 1988; Mulugeta and Koyi, 1992; Koyi, 1995; Gutscher et al., 1998; Dominguez et al., 2000; Adam et al., 2005; Konstantinovskaia and Malavieille, 2005]. Experiments where the layers are overlying a rigid basement and are subjected to horizontal shortening produce a self-similar accretionary prism analogous to accretionary prisms formed along subduction zones or in intracontinental fold-and-thrust belts [Chapple, 1978; Davis et al., 1983; Lallemand et al., 1994; Gutscher et al., 1998]. These experiments lead to the formation of imbricate thrust sheets that gradually accrete to the wedge as the detachment propagates forward. In the absence of cohesion this process and the resulting geometries are scale-independent. However, given the estimate of the cohesion of the material used in this experiment ( $C_o < 50$  Pa) and the typical cohesion of crustal rocks ( $C_o > 20$  MPa) [Lallemand et al., 1994; Schellart, 2000], the scaling factor can be estimated to about  $10^5$ . Accordingly, 1 cm in the model is equivalent to about 1 km in nature.

[7] The model box is 20 cm wide and 100 cm long and is equipped with transparent sidewalls treated to reduce fric-

**Table 1.** List and Definition of the Variables Used in the Analysis

Variable	Definition
$h$	total thickness of the layers
$\phi$	measured basal friction angle
$\phi_b$	theoretical basal friction angle
$\phi_s$	internal friction angle of the sand mass
$\phi_g$	internal friction angle of the glass beads
$U$	local uplift relative to the footwall
$V$	horizontal shortening
$x$	horizontal coordinate
$z$	vertical coordinate
$\theta(x)$	local dip angle
$U_{\max}$	maximum uplift rate
$r$	shortening rate
$\theta_{\max}$	maximum dip angle of the fault
$\lambda$	horizontal displacement gradient
$\alpha_i$	vertical displacement gradient
$\psi$	simple shear angle
$r'$	slip on the fault in case of simple shear
$\beta$	acquired dip due to an incremental shortening

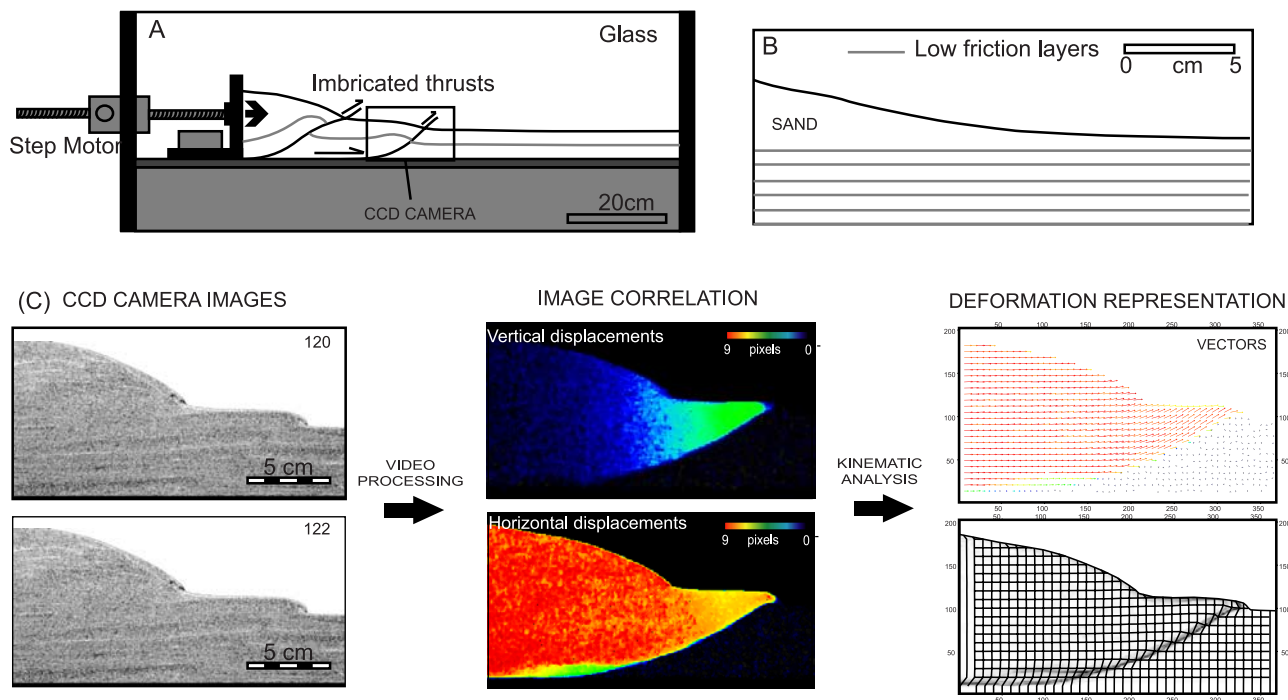


**Figure 3.** (a) Experimental setup. To build the model, granular materials were sprinkled into a 20 cm wide and 100 cm long box equipped with transparent sidewalls, similar to the experimental setup used by *Dominguez et al.* [2000]. The sand layers slide on a horizontal ( $\beta = 0$ ) basal polyvinyl chloride (PVC) plate, 2 cm thick. Initially undeformed sand mass is compressed and deformed by a backstop moved by a step motor. A CCD camera takes pictures (6.3 megapixels with a spatial resolution of  $0.04 \text{ m}^2$ ) with a constant time step corresponding to 0.2 mm (equivalent to 2.7 pixels) of shortening between two successive images. (b) Initial conditions. Five low-friction glass bead layers are interlayered with the sand layers. (c) Summary of the optical flow technique for measuring displacements. The numerical video image at step 122 is compared to the one at step 120. The displacement field is computed from the optical flow technique as described in the text. The incremental displacement field is represented by vectors or by a deformed grid. Also shown is the second invariant of the strain tensor ( $I_2 = \frac{1}{2}[\text{tr}(\varepsilon)^2 - \text{tr}(\varepsilon^2)]$ , where  $\varepsilon$  is the deformation tensor) in gray scale to emphasize zones of strain localization.

tion [*Dominguez et al.*, 2001]. The model comprises 6 sand layers, each 6–7 mm thick, intercalated with 5 glass bead layers, each 2 mm thick. The total model thickness,  $h$ , is 4.8 cm. We use this layering to simulate natural lithologic intercalations and stratigraphic discontinuities, and to facilitate layer parallel shear, a process which is thought to be key to folding of sedimentary layers at the natural scale.

[8] The sand and glass bead layers are deformed in front of a moving backstop activated by a step motor at a constant velocity of  $235 \pm 10 \mu\text{m}$  per minute (1.4 cm/h) (Figure 3). The cohesion and friction angle of the materials was provided by the manufacturers (SIFRACO and EYRAUD) and was also measured in our laboratory [*Krantz*, 1991; *Jolivet*, 2000; *Schellart*, 2000]. The sand has a fluvial origin with irregularly rounded grain shapes and sizes from 150 to 300  $\mu\text{m}$ . Its internal friction angle is  $30^\circ$  to  $35^\circ$  ( $\tan\phi_s = 0.6$  to  $0.7$ ) and its cohesion is low ( $C_0 < 50 \text{ Pa}$ ). The glass beads are  $\text{SiO}_2\text{-Na}_2\text{O}$ , cohesionless microspheres with grain sizes ranging from 50 to 150  $\mu\text{m}$  and an internal friction angle between  $20^\circ$  and  $25^\circ$  ( $\tan\phi_g = 0.35$  to  $0.45$ ). The model is built on a 2 cm thick horizontal ( $\beta = 0$ ) polyvinyl chloride (PVC) plate. The basal friction along the sand/unpolished PVC interface is  $21 \pm 4^\circ$  ( $\tan\phi_b = 0.38$ ) [*Jolivet*, 2000].

[9] Our experimental setup was designed so as to measure, with the maximum possible accuracy, the deformation at the tip of the basal detachment and the formation of a new thrust fault at the front of the wedge. In order to avoid episodic reactivation of older internal faults and force the deformation to be localized at the very front of the wedge, we started the experiment with a  $10^\circ$  predeformation sand wedge. In experiments run with the same layering as the one described here we observed the formation of a wedge with a slope of  $8\text{--}9^\circ$ , which is approximately the critical slope of about  $8^\circ$  of a homogeneous wedge predicted from the critical wedge theory given the value of the basal friction angle,  $\phi_b$ , of  $21^\circ$  and the value of the internal friction angle,  $\phi_s$ , of  $30^\circ$  for the sand mass [*Davis et al.*, 1983]. This shows that the layering does not modify significantly the mechanical behavior of the accretionary wedge and that coulomb wedge theory can still be applied.

[10] We focus on the foreland edge of the wedge, which grows by the forward propagation of the basal décollement. This part of the experiment is located about 15 cm from the backstop and, to ensure maximum spatial resolution, is the only portion of the experiment monitored with the video system (box in Figure 3a). By comparing the imposed displacement of the backstop with displacements measured

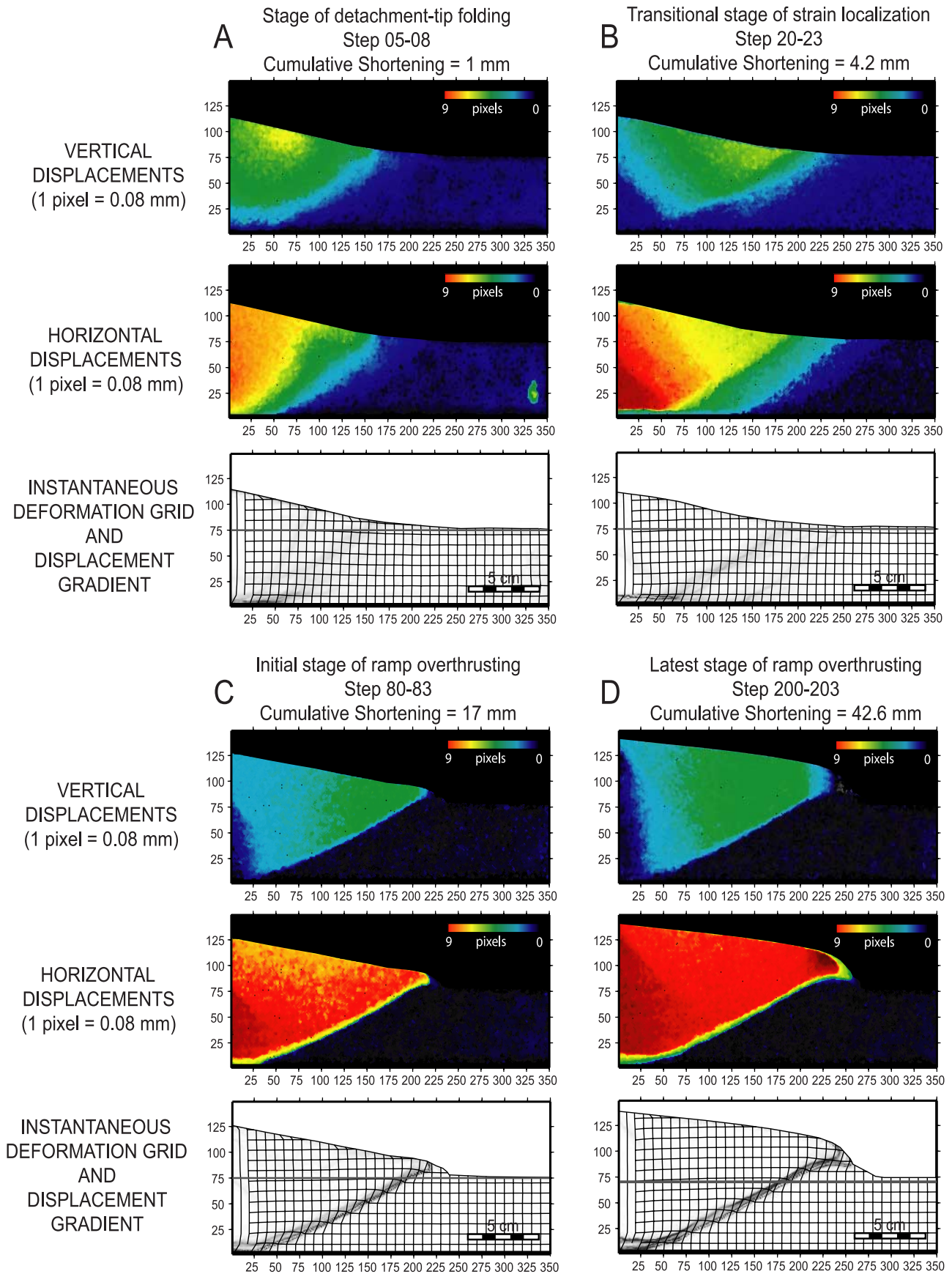


Figure 4

within the zone monitored by the video system, we find that during the selected experiment about 98% of the shortening is absorbed by internal deformation within the monitored frame. Photographs are taken with a constant sampling rate of 1 image/minute with a 6.3 megapixels CCD camera. The pixel size is 80 by 80  $\mu\text{m}^2$ . Given that the backstop velocity and the sampling rate are constant, the incremental shortening between two successive images is constant and equals  $235 \pm 10 \mu\text{m}$ . The displacement field between two successive images is measured from the optical flow technique, which was introduced by *Horn and Schunck* [1980] and which is commonly used in remote sensing and image processing for robotic applications. It applies to images with a brightness pattern that evolves only due to deformation of the medium, as is the case of our experiment. The technique allows for a subpixel accuracy and appears more powerful than more recent correlation techniques such as particle imaging velocimetry [*Adam et al.*, 2005]. It is based on the fact that the image  $F$  at time  $t + dt$  can be written

$$F(t + dt) \approx F(t) + \nabla F(t)dX, \quad (2)$$

where  $dX$  is the displacement field and  $\nabla F(t)$  is the spatial gradient of image  $F(t)$ . Equation (2) is only an approximation because higher-order terms in the Taylor-Lagrange development are neglected. The gradient is estimated from Rider's method [*Press et al.*, 1995]. The technique was first applied to the analysis of sandbox experiments by *Dominguez et al.* [2001].

[11] The displacement field varies smoothly and the signal-to-noise ratio is better when it is measured over few images (typically over two to three images). The correlation window is  $32 \times 32$  pixels, and is moved by increments of 8 pixels across the whole image. The displacement field thus contains  $350 \times 149$  independent measurements, with a sampling (or spatial) resolution of  $640 \mu\text{m}$ . On the basis of calibration tests, errors on measurements are statistically estimated to be less than 5%. The horizontal and vertical components of the displacements are plotted separately and used to generate various representations such as displacement vectors or incremental deformation of a virtual grid (Figures 3 and 4). Because the measurements are made from pairs of images separated by variable time lags, incremental displacements are normalized by dividing them by the number of time steps (one step corresponding to two successive images). Displacements are thus expressed in millimeters per step (mm/step), where a step corresponds to a shortening of  $235 \pm 10 \mu\text{m}$ , and are thus equivalent to normalized velocities. For our analysis we examine profiles across the horizontal and vertical displacement fields at different depths above the décollement.

[12] Surface processes are not simulated in the model. Therefore the analogue experiment does not directly repro-

duce growth strata or deformed terraces. However, the mathematical description of folding derived from this experiment, as detailed below, can easily be used to simulate the expected geometry of growth strata or terraces [*Simoès et al.*, 2007b; *Daëron et al.*, 2007].

### 3. From Detachment Tip Folding to Ramp Overthrusting

[13] Deformation within the domain covered by the imaging system starts to become significant only after about image 10, which corresponds to 2.3 mm of shortening, or 5% of the initial thickness of the sand layers ( $h/20$ ). Prior to this, deformation is entirely accommodated closer to the backstop, outside the area covered by the camera. Following this initial phase of shortening, the evolution of deformation can be divided into two main stages that are the focus of our analysis. The first stage comprises distributed deformation and tip line folding above the foreland edge of the horizontal basal detachment. The second deformation stage occurs after a brief transitional phase of strain localization and consists of upward propagation of the detachment tip and of the formation of a mature frontal thrust ramp. Hanging wall material is subsequently transported along this new fault surface.

[14] During the first stage of deformation, horizontal velocities decrease linearly with distance away from the backstop, and vertical velocities show a nearly symmetrical, trapezoidal pattern of uplift (Figure 5a). We separate the uplift pattern into domains in which incremental uplift varies linearly with horizontal distance and interpret the boundaries of these domains as fold axial surfaces. The position of each of these surfaces was determined by the maximum change in slope of the uplift rate versus distance and is calculated in several different horizons (Figure 6). The analysis of the evolving velocity field during this stage of deformation allowed us to study the kinematic behavior of the four identified axial surfaces.

[15] The two outer axial surfaces (labeled 1 and 4 in Figure 7) initiate and remain at a constant position throughout the first stage of deformation. Axial surface 4 marks the frontal limit of the deforming zone and appears to be fixed to both the footwall and hanging wall, essentially acting as a foreland pin line. The discontinuity in the horizontal velocity field places this pin line 30 mm further to the foreland than the discontinuity in the vertical displacement field, suggesting there is a measurable, but small volume loss in the foreland adjacent to the growing fold. We believe this volume loss is a specific feature of the analogue model, and most likely results from a reorganization of sand grain packing that would not occur in a natural setting. The most hinterland axial surface (labeled 1 on Figure 7) is also fixed to the footwall, but hanging wall material appears to migrate through it as shortening continues (Figure 7b). Axial surfa-

**Figure 4.** Incremental displacement field and strain measured during (a) the stage of detachment tip folding (between steps 05 and 08, cumulative shortening 1 mm), (b) the transitional stage of strain localization (between steps 20 and 23, cumulative shortening 4.2 mm), and (c and d) the stage of ramp overthrusting (between steps 80 and 83, cumulative shortening 17 mm and between steps 200 and 203, cumulative shortening 42.6 mm). For each of these plots the cumulative horizontal shortening is indicated. Note that in the early stage, deformation is not localized. After a cumulative shortening of about 6 mm it localizes on a frontal ramp connecting the basal décollement with the surface.

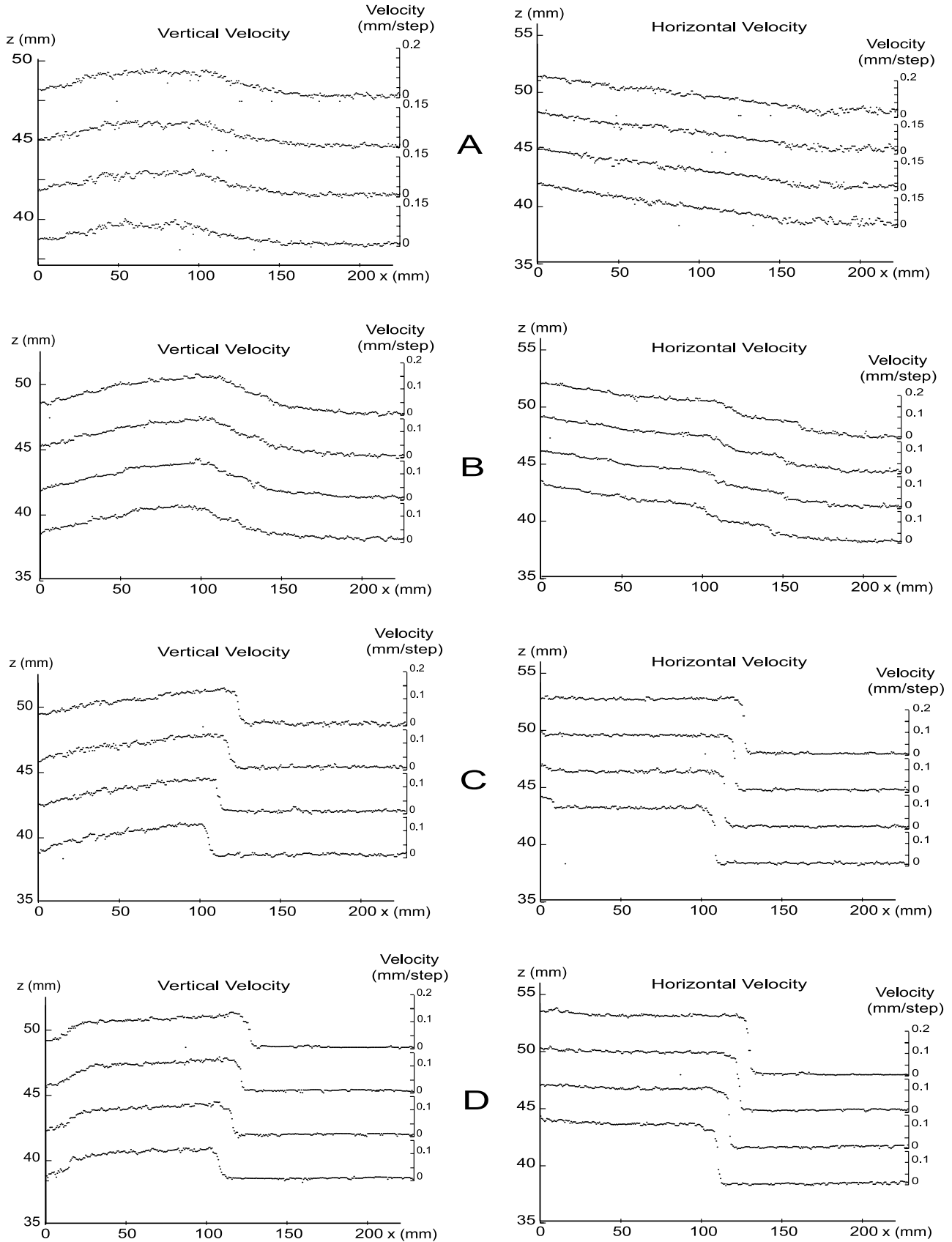
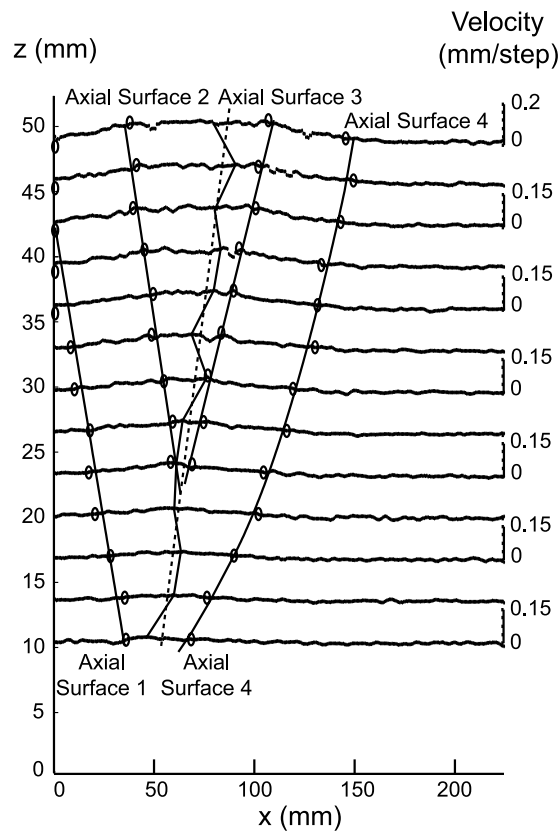


Figure 5





**Figure 6.** Uplift rates during the detachment tip folding stage (between steps 10 and 12), measured along profiles at different depths. For each profile, the position of the ordinate axis indicates the depth at which the profile is examined. The position of the various axial surfaces determined from the break in slope (circles) is indicated, as well as the locus of the maximum uplift rate on each profile (dark line). The three most hinterland axial surfaces (1, 2, and 3) are reasonably well fit by a straight line, suggesting a linear dependency with depth. A straight line also fits reasonably well the abscissa corresponding to the maximum uplift rates on each profile. The most frontal axial surface can be adjusted with a second-order polynomial.

ces 2 and 3 immediately bound the fold crest, and are only recognized by discontinuities in the vertical velocity field (Figure 7a). These surfaces move slightly and/or change orientation during increasing shortening, suggesting they are loosely fixed to the hanging wall (Figure 7b). Throughout the first stage of deformation, the sand layers in the fold limbs rotate and experience some component of pure shear.

[16] The end of the first deformation stage is marked by a short transient stage of strain localization that precedes ramp overthrusting. In this particular experiment at a

cumulative shortening of 4.2 mm, the deformation gradually focused along two discrete shear bands, each dipping approximately  $25^\circ$  toward the hinterland. Although the shear bands occur as prominent features in the horizontal displacement field (Figures 4b and 5b), they accommodate less than 30% of the total deformation. With continued shortening the more internal shear band, which approximately coincides with axial surface 3 defined in the vertical displacement field, tends to become dominant and evolves into a well-developed thrust fault connecting the basal décollement to the surface (Figures 4c and 5c). Formation of this frontal thrust ramp induces a significant change of model deformation kinematics and marks, then, the end of the fault tip stage.

[17] At the beginning of the second stage of deformation, when the cumulative shortening typically exceeds about 6 mm, or roughly 13% of the initial thickness of the sand layers ( $h/8$ ), a prominent thrust ramp exists at the front of the sand wedge (Figures 4c, 4d, 5c, and 5d). The footwall subsequently stops deforming and all the horizontal shortening is taken up by slip on this shear zone, which acquires a stable sigmoid geometry. The hanging wall is then thrust over the ramp with some internal deformation to accommodate the flat-to-ramp geometry. Axial surface 1 remains fixed to the footwall whereas axial surface 2 is fixed to the hanging wall and is passively transported along the fault. Thereafter, the velocity field remains constant, because the fault geometry ceases to evolve. In general, the kinematics of the second stage of deformation is very similar to those of a simple ramp anticline as predicted by fault bend folding theory [Suppe, 1983] (Figure 2a).

[18] Figure 8 shows how the maximum uplift rate,  $U_{\max}$ , varies during a complete experiment. Before deformation gets localized, maximum uplift rate is observed to increase gradually and may be as large as twice the value predicted by fault bend folding theory:

$$U_{\max} = r \sin \theta_{\max}, \quad (3)$$

where  $r$  is the shortening rate and  $\theta_{\max}$  is the maximum dip angle of the fault, here about  $25^\circ$ . This result is consistent with little internal deformation within the sand layers and demonstrates that care must be taken when inferring shortening rates from uplift rates during the detachment tip folding phase of deformation, that is prior to the formation of the thrust ramp.

#### 4. Analytical Representations of Surface Uplift and Horizontal Velocity During Fault Tip Folding

[19] Vertical displacements are described from linear segments connecting the four axial surfaces (Figures 5 and 7). The axial surfaces are generally well defined from the

**Figure 5.** Horizontal and vertical displacement rates measured along profiles run at different depths during (a) the detachment tip folding stage (between steps 10 and 12, cumulative shortening 2.1 mm), (b) the transitional stage of strain localization (between steps 20 and 23, cumulative shortening 4.2 mm), and (c and d) the stage of ramp overthrusting between steps 50 and 53 (cumulative shortening 10.6 mm) and between steps 150 and 153 (cumulative shortening 32 mm). The abscissa axis is positioned at the depth at which each profile is run.

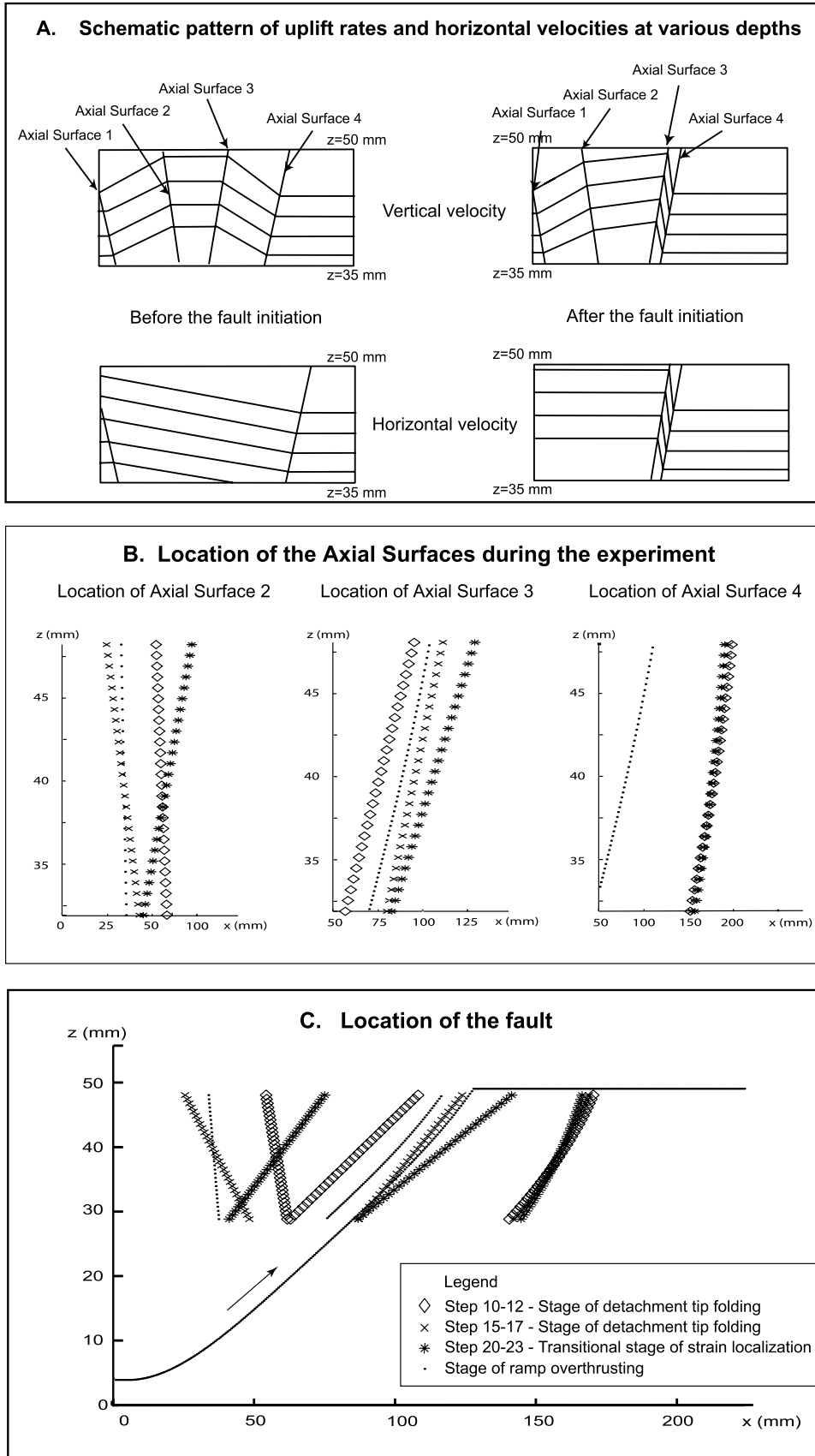
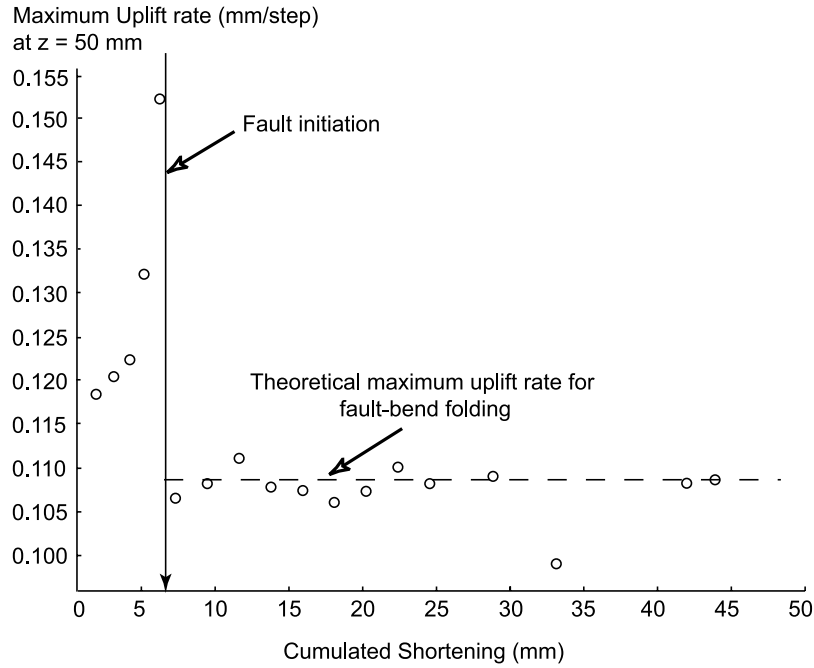


Figure 7



**Figure 8.** Maximum uplift rate (at  $z = 50$  mm) as a function of cumulative shortening. In the early stage of the experiment, during the stage of detachment tip folding and the transitional stage of strain localization, before deformation gets strongly localized, the maximum uplift rate increases gradually. Once deformation is localized on a frontal ramp the maximum uplift rate is independent of the cumulative shortening and is simply  $U_{\max} = r \sin \theta_{\max}$ , where  $r$  is the shortening rate and  $\theta_{\max}$  is the maximum dip angle of the fault, about  $25^\circ$ .

profiles run at elevations above about 25 mm but are generally more difficult to track closer to the décollement where vertical displacements are smaller. The geometry of the first axial surface is not always well determined since it extends outside the image. Horizontal displacements vary linearly with horizontal distance between two bounding axial surfaces (Figure 5).

[20] During the first detachment tip folding stage of deformation, we observe that horizontal velocity,  $V$ , decreases linearly with  $x$ , and tapers to zero at  $\sim 30$  mm ahead of the axial surface 4 (Figures 4a and 5a). Incremental horizontal displacements can be described by

$$V = r(z)(1 - \lambda(z)x), \quad (4)$$

where  $r(z)$  is the horizontal incremental shortening at the back of the structure and  $\lambda(z) = 1/W_h(z)$ , with  $W_h(z)$  the distance between axial surfaces 1 and 4.

[21] Because the maximum uplift rate scales linearly with the initial datum elevation,  $z$  (Figure 9), we may write

$$U_{\max} = \gamma z + \mu. \quad (5)$$

In the ideal case of a zero thickness décollement, the parameter  $\mu$  should be equal to zero because no uplift would

be observed at the level of the décollement. This parameter  $\mu$  is not zero in our experiment because the décollement is a shear zone of finite thickness. In addition, as shown in Figure 9, the uplift profile at each depth obeys

$$\frac{\Delta U / U_{\max}}{\Delta X} = \eta, \quad (6)$$

where  $\Delta U$  is the difference in uplift at two points separated by a horizontal distance  $\Delta X$ . Since  $U_{\max}$  depends linearly on  $z$ , we get

$$\frac{\Delta U}{\Delta X} = \eta(\gamma z + \mu), \quad (7)$$

which implies that the pattern of incremental uplift in each dip domain between the axial surfaces can be written as

$$U = \eta(\gamma x z) + \mu x + \delta(z), \quad (8)$$

where the parameters  $\eta$ ,  $\gamma$ ,  $\beta$ ,  $\delta$  depend on the considered dip domain. This simple parameterization yields a good fit

**Figure 7.** (a) Schematic pattern of uplift rates and horizontal velocities at various depths. As deformation increases, the positions of the axial surfaces evolve, in particular axial surfaces 3 and 4 nearly coalesce to define a localized shear zone corresponding to the frontal ramp. (b) Location of the three frontal axial surfaces during the experiment. (c) Geometry of the frontal fault which forms after about 6 mm of shortening together with the positions of the axial surfaces determined from the vertical displacements.

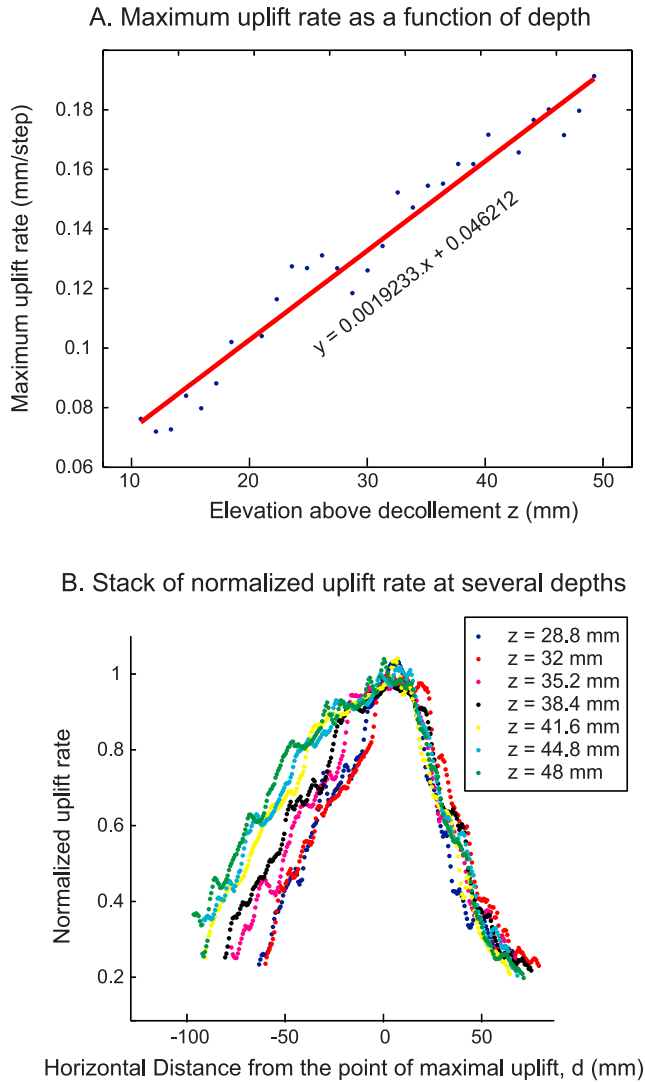


**Figure 9.** (a) Maximum uplift rates as a function of elevation above the décollement during the stage of detachment tip folding (values from steps 10–12). A linear function (dashed line), as proposed in equation (5), provides a good fit. (b) Normalized uplift rates at several depths. Uplift rates are normalized by the value of the maximum at each depth (values from steps 10–12).

to the data (Figure 10). For easier use, equation (8) can be rewritten for each domain,  $i$ ,

$$U(x, z) = U(x_i, z) + \alpha_i z(x - x_i), \quad (9)$$

where  $\alpha_i$  is a constant parameter for each dip domain  $i$  considered. The term  $U(x_i, z)$  corresponds to the vertical increment within the dip domain ( $i - 1$ ) at the horizontal position  $x_i$  of the axial surface shared by consecutive dip domains  $i$  and ( $i - 1$ ), and allows for continuity of vertical displacements from one dip domain to the next one. Since the surface area of the deforming domain is approximately constant,  $U(x, z)$  depends uniquely on the parameters in equation (9) and on the position of the two axial surfaces

defined from the horizontal displacements. The predicted horizontal velocity obtained from this assumption is in quite good agreement with the measurements (Figure 10a). During the transition from the initial stage of distributed deformation to ramp anticline formation, horizontal displacements need a more complex formulation. A reasonable fit to the data is however still obtained by assuming again mass conservation and linear functions between axial surfaces (Figure 10b).

## 5. Comparison With Other Models of Fault-Related Folding

### 5.1. Comparison With an Elastic Dislocation Model

[22] We discuss first the possibility of modeling the observed kinematics from dislocations embedded in an elastic half-space [Okada, 1985]. Although the deformation observed in the experiment is not recoverable, hence non-elastic, it might be argued that this kind of model might provide a reasonable approximation to the velocity field [e.g., Ward and Valensise, 1994]. Following Ward and Valensise [1994], we have imposed a coefficient of Poisson of 0.5 to insure conservation of volume. We found it impossible to correctly predict simultaneously the vertical and horizontal velocities from this approach (Figures 11 and 12). We reached the same conclusion while analyzing the stage of fault tip folding and the stage of ramp overthrusting. In both cases, we find that slip rates derived from modeling the uplift pattern using elastic dislocations would be overestimated. It is generally possible to obtain a reasonable fit to the profile of uplift rate at the surface, or in a natural case to deformed seismic reflectors from this approach, but inferences on fault geometry at depth and on any displacement rates might be biased and should be considered with caution.

### 5.2. Comparison With Trishear Folding

[23] The kinematics observed in our experiments show similarities with the trishear fault propagation model [Erslev, 1991]. In the trishear model, a single fault expands outward into a triangular zone of distributed shear. An unlimited number of velocity fields and shapes of the triangular zone can be generated by varying the propagation-to-slip ratio ( $P/S$ ), which determines how rapidly the tip line propagates relative to the slip on the fault itself [Allmendinger, 1998; Allmendinger and Shaw, 2000; Zehnder and Allmendinger, 2000].

[24] In the first phase, the deformation pattern results from distributed shear in a domain delimited by the two bounding hinges. Shear is not homogeneous and the deforming domain is not exactly triangular. As formulated in previous studies, the trishear model requires in addition that the fault dip angle lies between the dip angles of the two boundaries of the triangular zone of distributed shear. As a result, it is not possible to model distributed shear above the tip of a décollement. Hence the model does not apply directly to the first phase. The trishear model might be adapted to that case but here we rather opted for the formulation described above (equation (4) and (9)), which ignores the propagation of the décollement.

[25] Deformation during the stage of frontal ramp propagation is close to a trishear fold mechanism although there

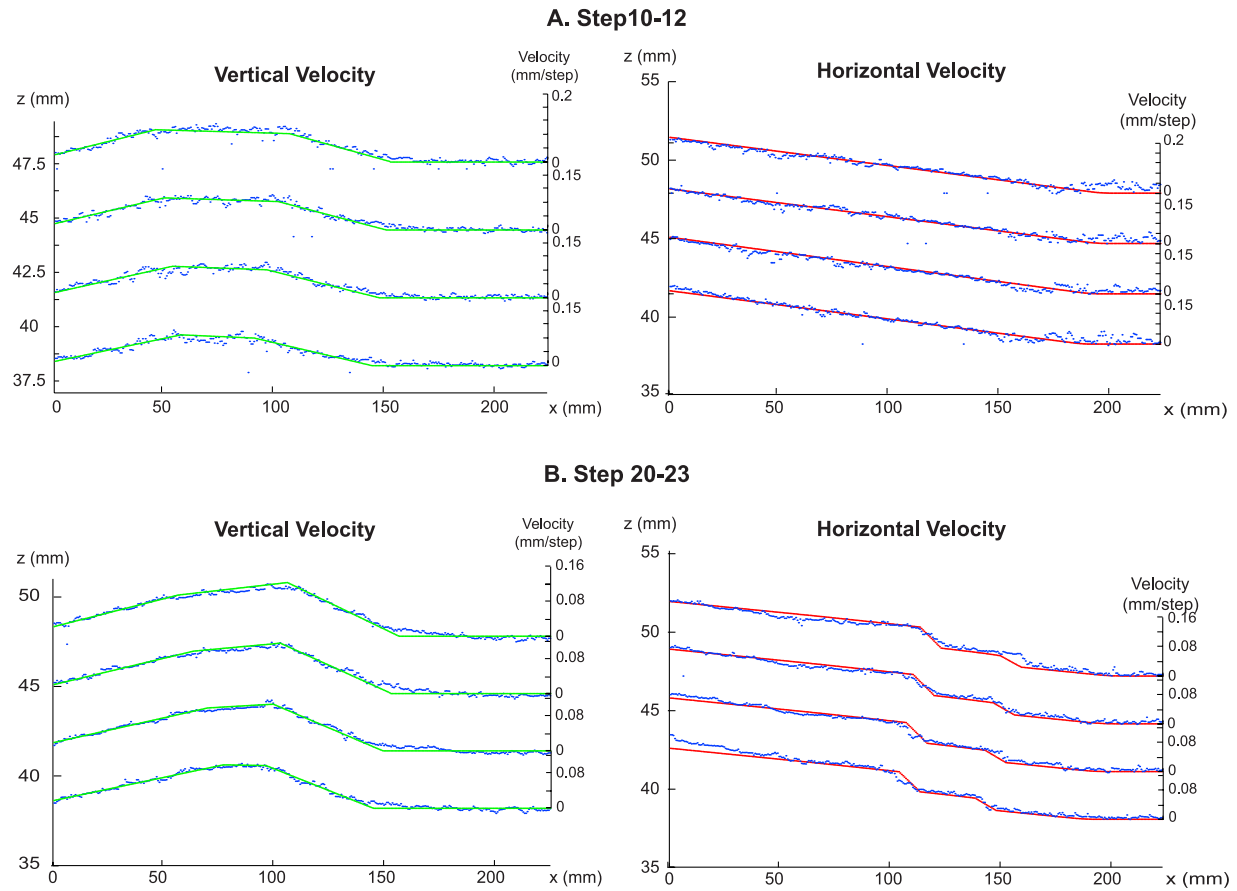


**Figure 10.** Comparison of the measured displacements (blue dots) with those predicted from the linear model detailed in text (red or green lines) before fault localization: (a) during the detachment tip folding stage (between steps 10 and 12) and (b) during the transitional stage of strain localization (between steps 20 and 23) (i.e., for a cumulative shortening lower than 6 mm). The RMS of the fit to the uplift rate is 0.012103 mm/step between steps 10 and 12 (computed for the profile at an elevation of 50 mm above the décollement). The fit to the horizontal velocities yields a RMS of 0.021771 mm/step between steps 10 and 12.

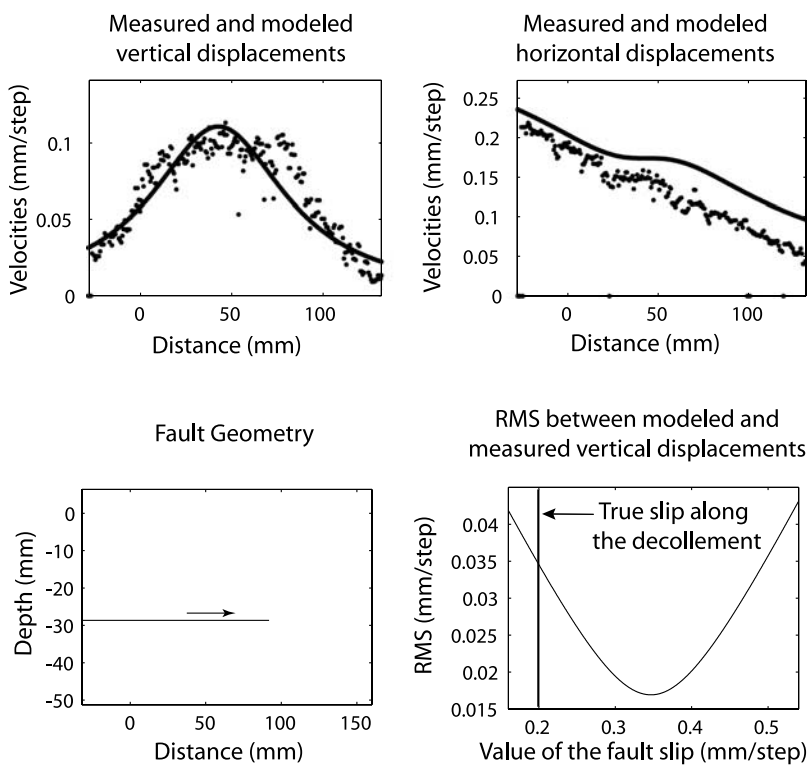


**Figure 11.** Results from dislocation modeling of observed vertical and horizontal velocities during the stage of detachment-tip folding (between steps 10 and 12) using the theory of a dislocation in an elastic half-space [Okada, 1985]. (top left) Measured (dots) and modeled (solid line) vertical displacements at the surface. (top right) Horizontal displacements extracted from the data (dots) and calculated (solid line). (bottom left) Shape of the fault used to calculate displacements. (bottom right) Value of the root mean square difference between observed and calculated vertical displacement as a function of slip rate on the décollement.

is no clear indication in our experiment of propagation of the tip of the ramp during this transient stage of strain localization (Figure 2, model B4).

### 5.3. Comparison With the Fault Bend Fold Model

[26] Once the frontal ramp has propagated up to the surface (when cumulative regional shortening exceeds  $h/8$ ) the system evolves toward a ramp anticline. In this case, the uplift rate pattern is fully determined by the shortening rate,  $r$ , and the fault geometry, which controls the position of the axial surfaces. A possible kinematic model would be that the hanging wall deforms by bedding plane slip according to the fault bend folding model [Suppe, 1983], which assumes conservation of the length and thickness of the sand layers. Here, we test whether this model can be used to model the kinematics of folding in the stage of ramp-anticline folding. In such a case, equation (1) would hold as soon as the sand layers become parallel to the fault, as pictured in Figure 13, and hence when the cumulative slip on the ramp exceeds  $U/\sin(\theta)$  (where  $\theta$  is the average dip angle of the fault). In the hanging wall, uplift rate depends on the dip of the fault at depth, which is equal to the local bedding dip angle. If the fault dip angle is  $\theta$  at the  $x'$  coordinate, at depth  $z$  the  $x$  coordinate where the bedding dip angle is  $\theta$ , is  $x = x' - z \tan(\theta)$  (Figure 13). The relation

between the horizontal displacement  $V(x)$  and the vertical displacement  $U(x)$  is then simply

$$V(x) = U(x) / \tan(\theta(x')), \quad (10)$$

where the fault dip angle is  $\theta(x')$  at point  $x'$  as defined above. To test the model, the fault shown on Figure 7c was determined from the measured strain field and adjusted from a fourth-order polynomial. The measurements rather suggest a shear zone with a finite thickness of the order of 3 mm. In order to improve the fit of the model and avoid having large misfits near the fault zone (which could artificially increase the RMS between the data and the predicted displacements), the predicted displacements were smoothed with a Gaussian function with a variance of 3 mm. We observe that this formulation provides a relatively good fit to the uplift rates, but the cumulative slip is less than the critical value,  $U/\sin(\theta)$  (RMS of  $10.9 \times 10^{-3}$  mm/step between steps 150 and 153). If this model were used to estimate shortening rate from the measured uplift rate in the experiment, it would underestimate the actual value by 8–10%. This shows that the ramp overthrusting stage of our experiment does not exactly obey the fault bend fold model, which can be explained by the fact that beds near the surface are not yet parallel to the thrust fault at depth.

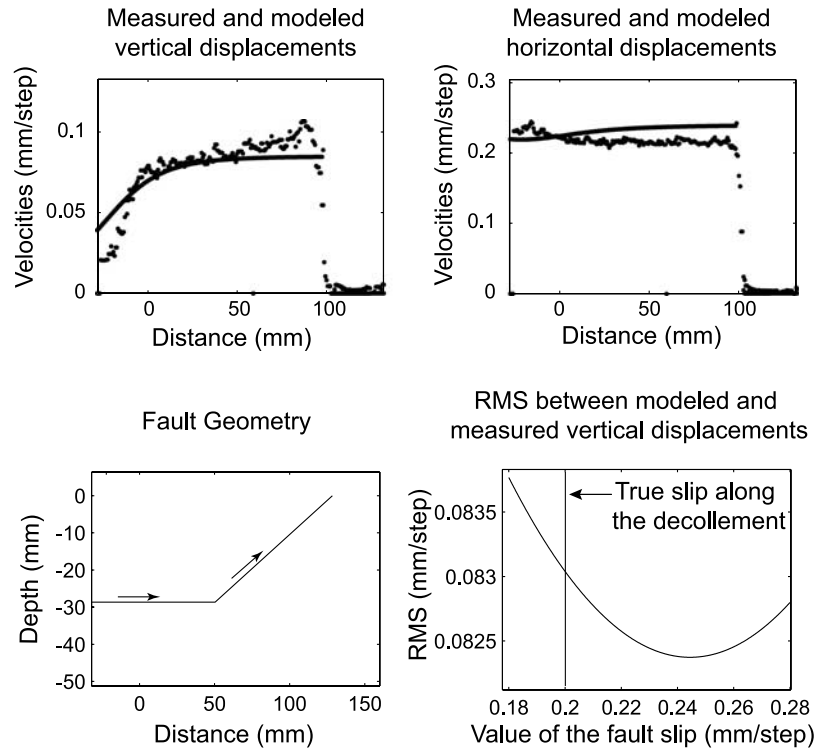


**Figure 12.** Results from dislocation modeling of observed vertical and horizontal velocities during the stage of ramp overthrusting (between steps 150 and 153). (top left) Vertical displacement at the surface extracted from the data (dots) and calculated (solid line). (top right) Horizontal displacements extracted from the data (dots) and calculated (solid line). (bottom left) Shape of the fault used to calculate displacements. (bottom right) Value of the square difference between observed and calculated vertical displacement versus the fault slip.

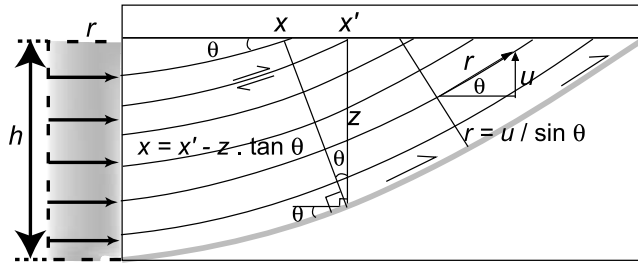


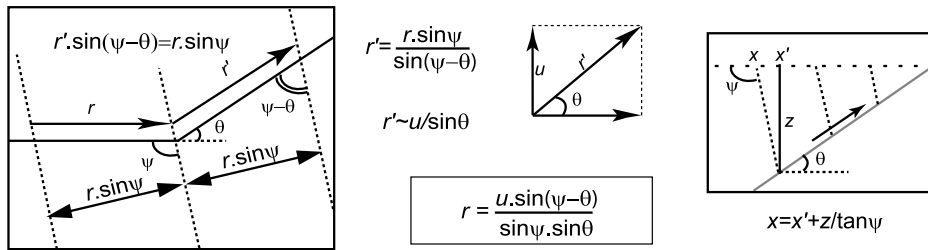
**Figure 13.** Diagram showing how the incremental uplift,  $u$ , of an initially horizontal horizon relates to incremental shortening in the case of a mature fault bend fold. The model assumes conservation of bed thickness and bed length, and the hanging wall deforms only by bed-parallel shear. Uplift is proportional to the sine of the fault dip angle, equivalent to the local bedding dip angle,  $\theta$ , and to slip along the fault (equation (1)). The assumption of constant bed thickness and length during deformation requires that at the point with abscissa  $x$  at the surface the bedding dip angle equals the fault dip angle at the point with abscissa  $x'$  along the fault.

**5.4. Comparison With a Simple Shear Folding Model**

[27] Another way to relate horizontal and vertical velocities along the profile after deformation gets localized is to assume that the hanging wall deforms by simple shear as pictured in Figure 14. This model obeys mass conservation only if the slip on the fault plane varies with the fault dip angle. Given that there is no line length change for lines parallel and perpendicular to the direction of simple shear, the projection of the velocity vector at any point in the direction perpendicular to the simple shear direction must be constant and equal to  $r \sin(\psi)$ , where  $r$  is the shortening at the back of the structure, and  $\psi$  is the simple shear angle defined in Figure 14. The slip  $r'$  on the fault is then expressed by

$$r'(x) = \frac{r \sin \psi}{\sin(\psi - \theta(x))}, \tag{11}$$

where  $\theta(x)$  is the local fault dip angle at point  $x$ .



Finite deformation of a level initially horizontal (dashed line)

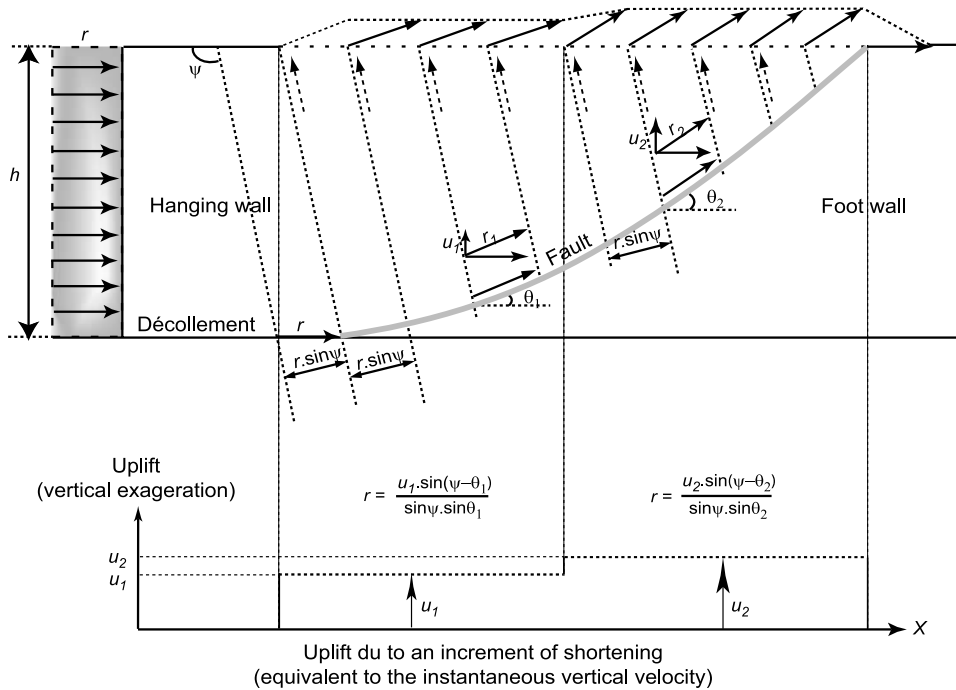


**Figure 14.** Sketch showing the relation between incremental shortening  $r$  and uplift of an initially horizontal horizon in the case of a ramp anticline with simple shear deformation of the hanging wall (simple shear angle  $\psi$ ). Conservation of area implies that slip has to vary along the fault.



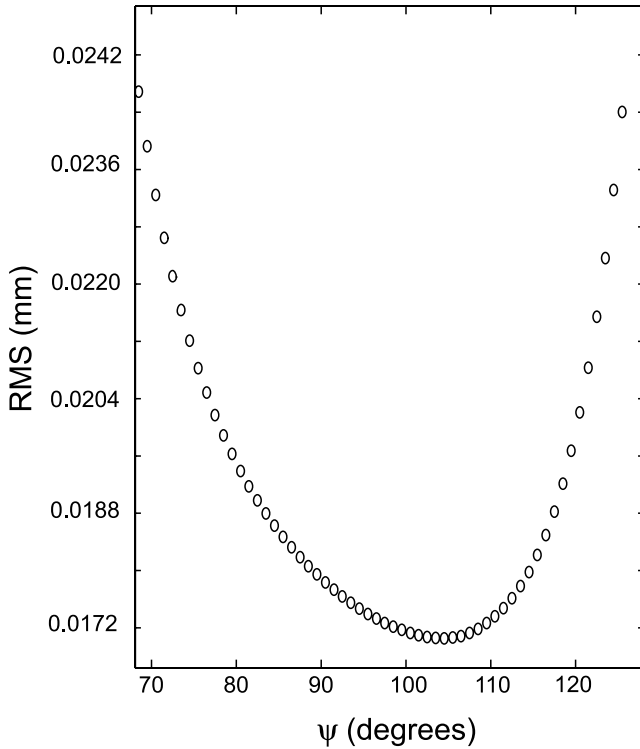


**Figure 15.** Plot showing how a model of ramp overthrusting with simple shear deformation of the hanging wall fits the observed uplift rates when the simple shear angle is varied (see sketch Figure 14). The best fitting shear angle is  $104^\circ$ . This result holds for all incremental displacements during this kinematic stage.

[28] The surface uplift at abscissa point  $x$  is then related to the uplift on the fault at a point  $x'$  with  $x = x' + z(x')/\tan \psi$  (Figure 14). The local uplift at the  $x$  coordinate can therefore be written as

$$U(x) = r'(x') \sin \theta(x'), \quad (12)$$

with  $\theta(x')$  the fault dip angle at point  $x'$ , and  $r'(x')$  the slip on the fault at the same point. Using (11) and (12), we can deduce the shortening  $r$  from the uplift profile

$$r(x) = \frac{U(x) \sin(\psi - \theta(x'))}{\sin \psi \sin \theta(x')}. \quad (13)$$

[29] Assuming simple shear deformation, the horizontal displacement  $V(x)$  along the section is then related to the vertical displacement  $U(x)$  and the fault dip angle at point  $x'$  according to

$$V(x) = \frac{U(x)}{\tan(\theta(x'))}, \quad (14)$$

where  $\theta(x')$  is the fault dip angle at point  $x'$  as defined above.

[30] This model predicts a sharp discontinuity of displacements across the fault which can lead to large local misfits when modeled and observed displacements are compared. To attenuate this effect, the displacements predicted from the model are smoothed with a Gaussian function with a variance of 3 mm.

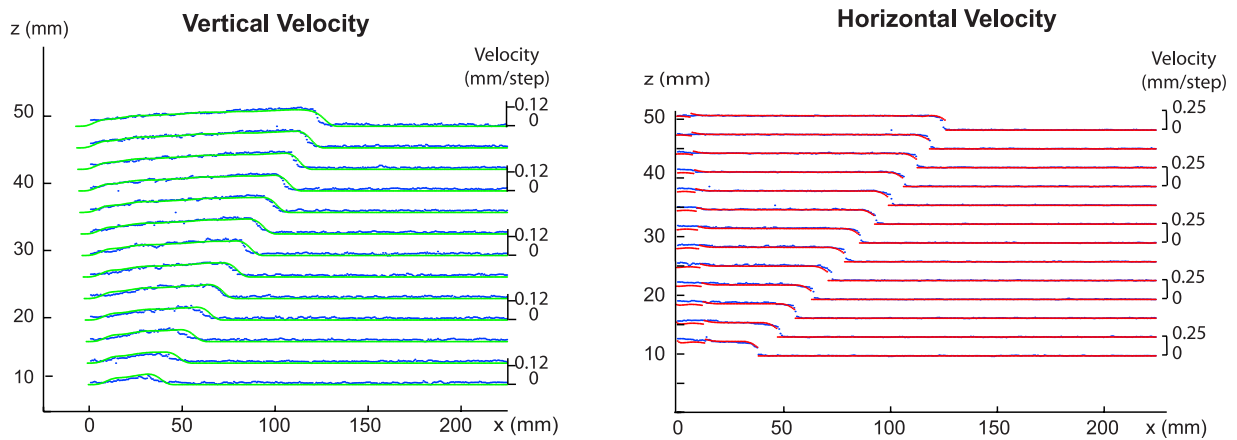
[31] We have next varied the simple shear angle,  $\psi$ , in order to maximize the fit to the observed displacements. It turns out that the best fit is found for an angle of about  $105^\circ$  (Figure 15). This modeling provides an excellent fit to the data (RMS of  $8.62 \times 10^{-3}$  mm/step for the vertical velocities and RMS of  $16.95 \times 10^{-3}$  mm/step for the horizontal velocities between steps 150 and 153), and reconciles both vertical and horizontal velocities (Figure 16), except at the back of the structure, where the fault is almost horizontal. Because the best fitting shear angle does not exactly bisect the detachment and the ramp dip angle, this direction of shear implies changes of the thickness and length of the sand layers during folding [Suppe, 1983]. Hanging wall units consequently thicken during their transport above the ramp, as also observed in other experiments [Maillot and Koyi, 2006; Koyi and Maillot, 2006].

## 6. Discussion on the Folding Mechanism Observed in the Analogue Experiment

[32] In this experiment folding results primarily from distributed plastic shear. After a critical value of shortening ( $h/8$ ), strain starts to localize and a frontal ramp develops. The ramp forms by strain localization close to a passive axial surface (the third one described above), where strain was able to accumulate during the first stage of folding (Figure 17). Because of this location, the tilted forelimb formed earlier becomes part of the footwall once the ramp is formed. Memory of the initial phase of fault propagation is thus preserved in the footwall and in the hanging wall from the tilted forelimb. Note that in the presence of erosion, once the system has become a ramp anticline, the memory of the initial phase of deformation in the hanging wall would be lost but preserved in the footwall (Figure 17). Such geometry has been observed across several piedmont folds north of the Tien Shan, which were inferred to have evolved from fault tip folds to fault bend folds [Avouac et al., 1993].

[33] Qualitatively, the behavior observed in this experiment is probably not specific to the particular setting of the experiment selected for this study. From a mechanical point of view, the axial surfaces are the expression of developing conjugate shear bands bounding a symmetrical pop-up structure (Figure 5b). After the localization of the favored fore-thrust shear zone (Figure 5c), the back-thrust shear zone is moving as part of the hanging wall on the ramp. The detail of the kinematics, however, must depend highly on the particular geometrical setup and material properties in the selected experiment. For example, it is probable that the amount of distributed deformation reached before localization is related to the onset of strain hardening and probably depends on factors such as the grain size and compaction [Lohrmann et al., 2003]. A complete mechanical analysis of

**Step 50-53**



**Step 150-153**

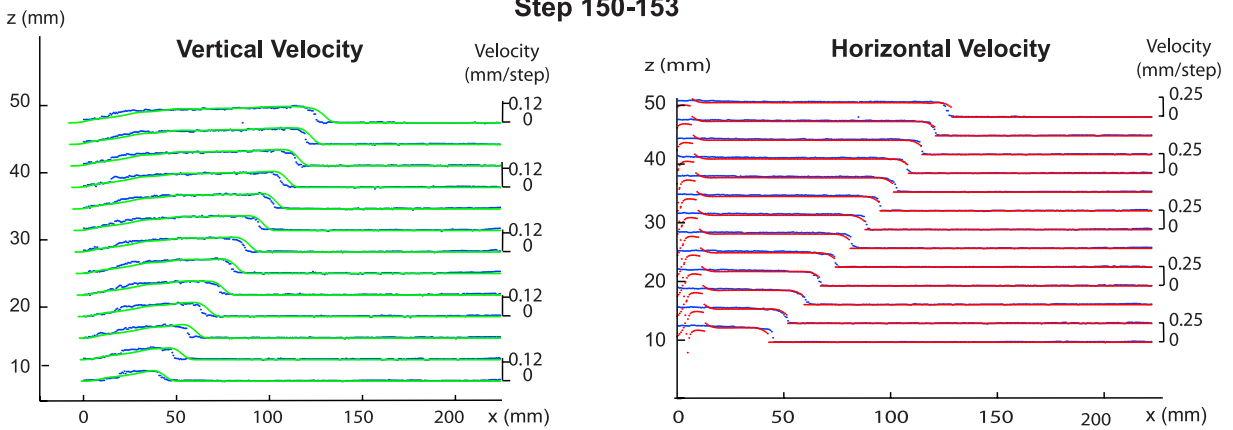


**Figure 16.** Comparison between observed horizontal and vertical velocities (blue dots) and the theoretical profiles (red or green lines) predicted from ramp overthrusting with simple shear deformation of the hanging wall for a shear angle of  $105^\circ$  as sketched in Figure 15. See text for details.

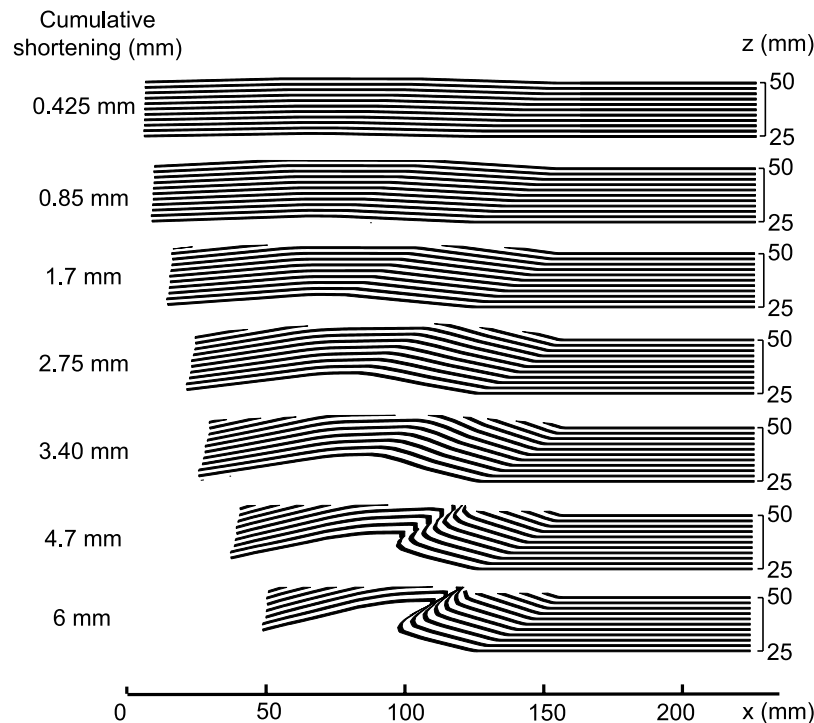


**Figure 17.** Finite deformation of layers initially horizontal, as computed from the proposed analytical approximation to the measured displacement fields. Horizontal and vertical displacements are exaggerated by a factor of 8 for readability. At each stage the cross section is obtained by applying incremental deformation to the previous stage. Erosion is not simulated, but displacements above the deformed surface after the first incremental shortening (0.2 mm) have not been modeled. The first 2 mm of shortening are not taken into account in this modeling. This choice implies a fault initiation after only 4 mm of shortening instead of 6 mm as discussed in the text. The phase of fault tip folding, up to 2.125 mm of shortening, assumes a stationary velocity field equivalent to that defined from steps 10 to 12 in the experiment. This corresponds to the phase of fault tip folding. The fold structure for a shortening of 2.75 and 3.4 mm, corresponding to the transitional stage of strain localization, was obtained from the velocity fields derived from steps 20 to 23 at the onset of strain localization within the sand layers. Above 4 mm of shortening we assume ramp overthrusting with simple shear deformation of the hanging wall as observed in the experiment from steps 50 to 53 (stage of ramp overthrusting).

the observed kinematics is beyond the scope of this study and would require a parametric study to elucidate the influence of each of the governing material properties and of the geometry (dependence on layer thickness, dependence on layering, etc.).

[34] During ramp overthrusting, we find a good fit between observed incremental displacements and the simple shear model assuming an optimal simple shear angle of  $105^\circ$  ( $\psi$  in Figure 14). Most of the shear occurs in the area where the detachment connects with the ramp. This zone thus appears as a migrating kink band, equivalent to a transient back thrust dipping by  $65^\circ$ . *Maillot and Leroy* [2003] have determined the optimal dip of the back thrust in such a fault bend fold that would correspond to a minimum of dissipated energy within the whole structure. The three sources of dissipation are due to frictional sliding on the ramp, on the back thrust and on the décollement [*Maillot and Leroy*, 2003]. As mentioned above, the basal coefficient of friction is estimated to  $21^\circ$  in this experiment. According to *Maillot and Leroy* [2003], the optimal dip of the back thrust would be  $30^\circ$  in this case, which implies a simple

shear angle of  $150^\circ$  quite different from that observed in the experiment. The system does not seem to respond as expected from the minimization of total dissipation. The observed kinematics does not conform either to the kinematics expected from conventional fault bend folding [*Suppe*, 1983]. This is because, despite the presence of the glass bead layers, layer-parallel longitudinal strain dominates over layer-parallel shear in this experiment.

## 7. Guidelines for the Analysis of Natural Fault Tip Folds

[35] We outline here how the fault tip fold kinematic model described above can be used to analyze natural folds. It is first assumed that cross-sectional area is preserved during folding. It should be recalled that a variety of mechanisms can lead to volume changes in analogue models, as observed in our experiment, or at the scale of natural folds such as tectonic compaction, dilatancy or pressure solution [*Koyi*, 1995; *Marone*, 1998; *Whitaker and Bartholomew*, 1999; *Lohrmann et al.*, 2003; *Koyi and*

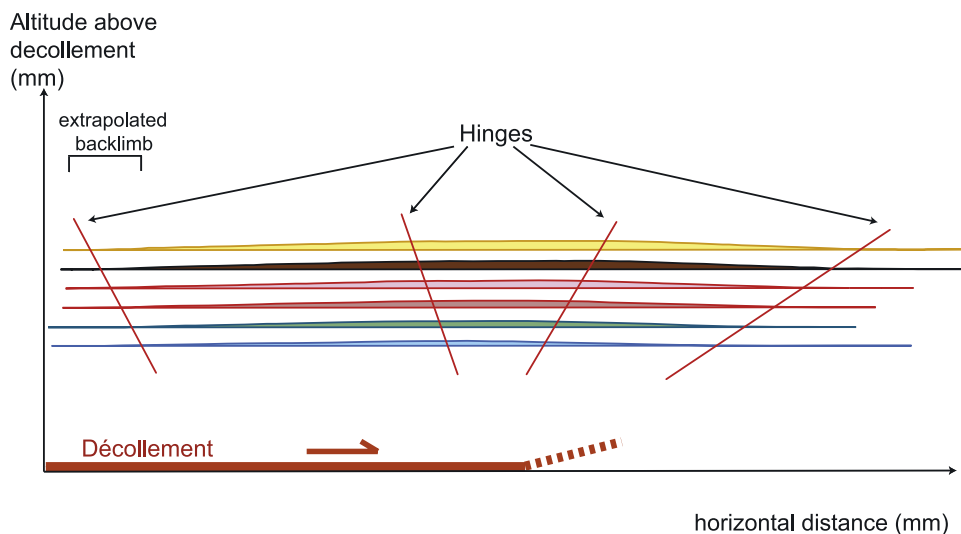


**Figure 18.** Structure of the modeled fold after an actual shortening of 3.4 mm corresponding to Figure 17. The geometry of the fold is not exaggerated here. The back limb has been extrapolated slightly outside the zone covered by our measurements. Each colored surface corresponds to the fold core area (or “excess area”) above the initial elevation of the considered strata. Inclined lines indicate axial surfaces delimiting domains of homogeneous finite dips as determined from this finite structure.

Cotton, 2004; Adam *et al.*, 2005]. The approach assumes in addition that the deformation field is stationary, meaning that all the axial surfaces remain fixed relative to the undeformed footwall. This is only a first-order approximation (Figure 7). Provided that these assumptions are correct, the analytic model makes it possible to retrieve the history of shortening across a fold from growth strata or from deformed fluvial terraces. This approach has been for the first time successfully applied to derive the kinematics of the Pakuashan anticline in west central Taiwan [Simoes *et al.*, 2007b], and an example of a subsequent application is available from Daëron *et al.* [2007]. First, the analytical expressions need to be calibrated based on the finite geometry of the fold (as imaged by seismic profiles for example). As an illustration and to test the hypothesis that deformation can be assumed stationary, we use the finite geometry after 3.4 mm of horizontal shortening, when localization of the fault has initiated at depth (Figure 18).

### 7.1. Relating Dip Angle and Shortening for Fault Tip Folds

[36] The key observation in the experiment is that uplift rate varies linearly within domains separated by axial surfaces (equation (9)), whereas incremental horizontal displacement varies linearly with a constant gradient over the whole fold area (equation (4)). The change in dip angle associated with an incremental shortening  $r$ , within a certain domain  $i$  is then given by:

$$\tan(\beta) = \frac{\alpha_i z r}{1 - \lambda(z)r}, \quad (15)$$

where  $\beta$  is the dip acquired after an incremental shortening  $r$ , in the case of a growth or a pregrowth stratum. This

relation can thus be used to infer the cumulative shortening recorded by tilted structural horizons or geomorphic surfaces, and if a set of pregrowth and growth strata are available, the history of folding can be retrieved.

[37] To calibrate the fold model parameters, the finite structure of the fold is used. Within each domain  $i$ , the coefficients in equation (15) might be determined from the observed structural dip angles of pregrowth strata (equivalent to  $\beta$  in equation (15)), provided that the cumulative shortening (equivalent to  $r$ ) and depth to the décollement ( $z$ ) are known. In practice, these latter two can be estimated from the excess area method [Chamberlin, 1910; Epard and Groshong, 1993]. Conservation of mass implies that the area  $A$  below a deformed level at an initial altitude  $z$  above the décollement equals the product  $zR$ , where  $R$  is the average total shortening of the layers below the considered horizon (Figure 1). By plotting  $A$  vs.  $z$ , one should obtain a linear relationship constraining both the cumulative shortening  $R$  and the depth to the décollement  $z$  (Figure 19). In the case of our analogue experiment, the retrieved plot is approximately linear but does not meet the condition that the excess area should be zero at the décollement (Figure 19). If the depth of the décollement was not known independently we would underestimate the décollement depth, and overestimate shortening by 55% (5.3 mm instead of 3.4 mm). This is a problem that has also been noticed in natural examples [Scharer *et al.*, 2004; Simoes *et al.*, 2007b], and décollement-parallel shear at the back of the fold, sometimes termed “back shear,” was advocated as a possible explanation. If back shear is assumed constant with depth, the function describing how the excess area varies with depth is parabolic (Figure 19a). In our case, a parabolic curve does not improve much the fit to the data, nor does it yield the right estimate of  $R$ . In fact, this explanation does not hold because the horizontal velocity field shows no

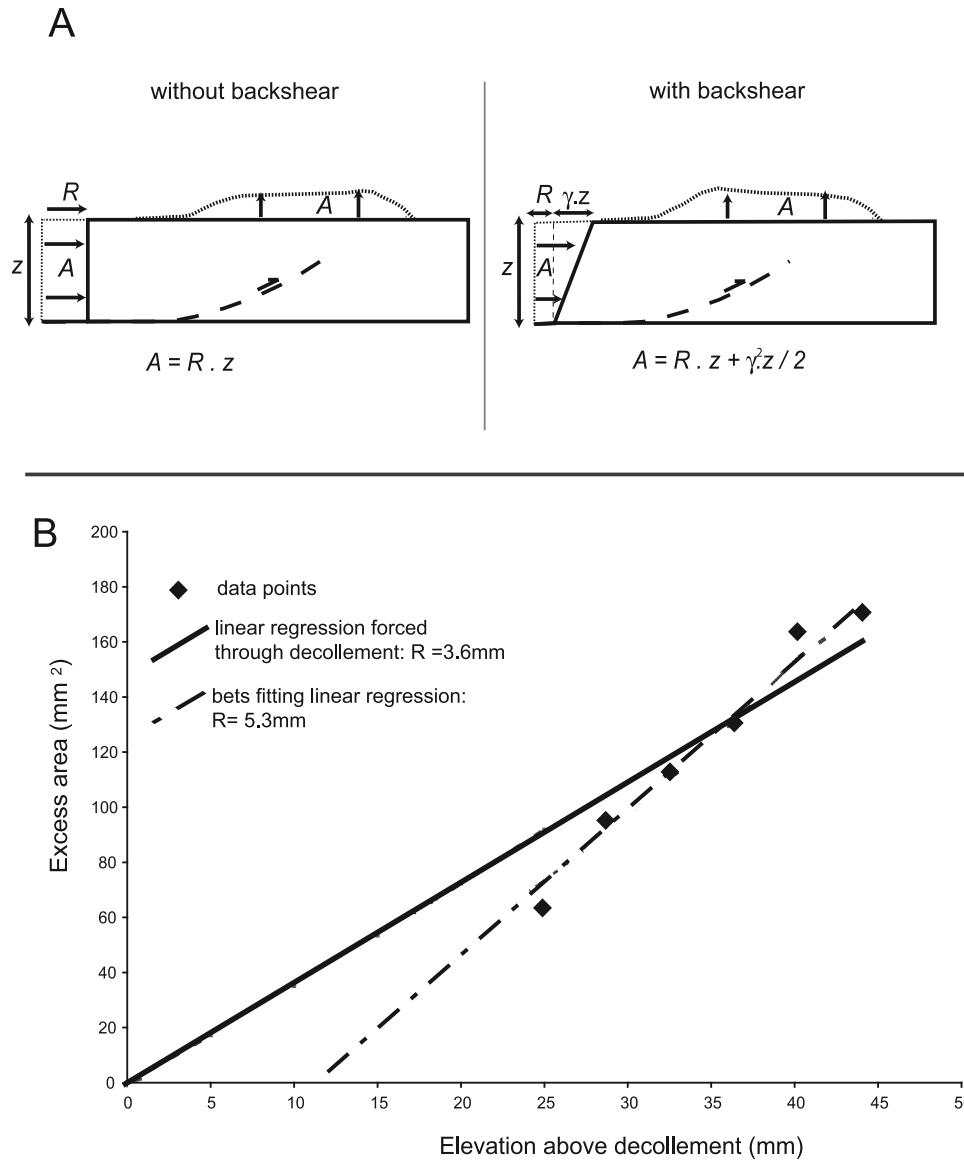


**Figure 19.** Excess area as a function of elevation above the décollement. (a) Without and with back shear. In the absence of any back shear, excess area,  $A$ , varies linearly with elevation above the décollement following Chamberlin’s law [Chamberlin, 1910]. In case of back shear, the relationship is no more linear. (b) Variations of excess area, as derived from Figure 18, as a function of elevation. A simple linear regression through the data yields a finite shortening of 5.3 mm too high and a décollement level too shallow. If the regression is forced through the origin to account for the known décollement, the estimated total shortening is close to the real value of 3.4 mm.

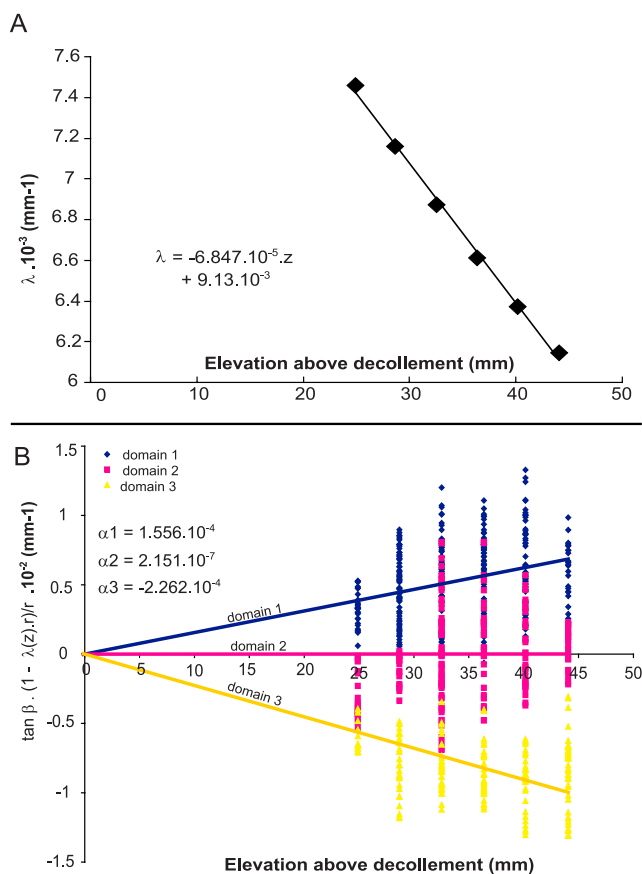


**Figure 20.** Parameters of the analytical formulations derived from the finite structure of the synthetic fold: (a)  $\lambda$  as a function of depth and (b)  $\alpha_i$  for each one of the three domains.

evidence for back shear. The discrepancy rather relates to the fact that the cross-sectional area is not conserved during the phase of fault tip folding. If we now impose the décollement depth by forcing the linear regression through the origin of the axis ( $A = 0$  at  $z = 0$ ), the excess area approach yields a total shortening of 3.6 mm close to the known experimental value. It therefore turns out that an independent constraint on the décollement depth is preferable when applying the excess area method to fault tip folds and that, without such information, the estimated shortening and décollement depth could be biased.

### 7.2. Determination of $\lambda$ and $\alpha_i$ Describing Incremental Displacements

[38] Once axial surfaces are defined,  $\lambda(z)$  may be easily determined from the width of the fold,  $W_h(z)$ , measured at several elevations above the décollement,  $z$ . Given the estimated depth to the décollement, the value of  $\alpha_i$  in each dip domain  $i$  can then be calculated from equation (15) (Figure 20). With these parameters, the synthetic fold geometry is reasonably well adjusted by the model (Figure 21). Mismatches most likely result from the fact that we did not allow for migration of fold axial surfaces over time, and that at the stage of fold development chosen for this test, strain localization has already begun. Also, the

model parameters have been calibrated from the finite structure, assuming a stationary deformation field.

### 7.3. Testing the Model Against Incremental Deformation

[39] The model calibrated from the analysis of the finite structure can be used to predict vertical and horizontal incremental displacements. It turns out that they compare relatively well with the incremental displacements measured from the analogue experiment itself, except for the most frontal zone where shear bands and compaction are observed at this advanced stage of fault tip folding (Figure 21). Excluding this domain, the observed discrepancy is within 10% of the incremental shortening imposed at the back of the fold, and it appears that the model usually tends to slightly underestimate the actual incremental deformation. The model derived from the finite structure seems thus adequate to describe the incremental growth of the fold, even at this advanced stage of fault tip folding. This validates the idea that incremental uplift or limb tilt that is recorded from terraces or growth strata can be analyzed from such simple analytical formulations to derive corresponding horizontal incremental shortening [e.g., *Simoes et al.*, 2007b].

## 8. Conclusion

[40] The experiment analyzed in this paper mimics the development of a fold growing over a propagating basal décollement which evolves toward a ramp-anticline. In the early stage, deformation is distributed leading to thickening and shortening of the sand layers. This mechanism results in gradual tilting of the forelimb and back limb. Up to about  $h/8$  of shortening, deformation of the medium is distributed and the fold grows as a result of thickening and shortening of the sand layers leading to limb rotation. Our measurements suggest that the fold kinematics can be described from a simple analytical formulation, which assumes that the velocity field is a linear function of depth and horizontal distance. Most importantly, the gradient of horizontal displacements is constant across the whole fold zone as long as strain does not localize. Once deformation is localized, a stable frontal ramp is formed and the system behaves as a ramp anticline. During this stage of deformation the measured displacements can be reproduced reasonably well assuming bed-parallel simple shear, as in the fault bend fold model, or simple shear parallel to a constant direction. We have observed the same qualitative behavior in other experiments similar to the one analyzed in detail in this study so that we can confidently state that the process described here is general, but we are unable at this point to assess how the observed kinematics relate to the mechanical properties of the sand and glass beads layers, or to the geometry of the experimental setup.

[41] On the basis of the kinematic model derived from this experiment, we propose some procedure to retrieve the fold kinematics from growth strata geometry or deformed geomorphic markers. This approach has been applied successfully for the first time to the analysis of the Pakuashan anticline, west central Taiwan [*Simoes et al.*, 2007b], and subsequently to detachment folds along the piedmont of the Tien Shan [*Daëron et al.*, 2007].

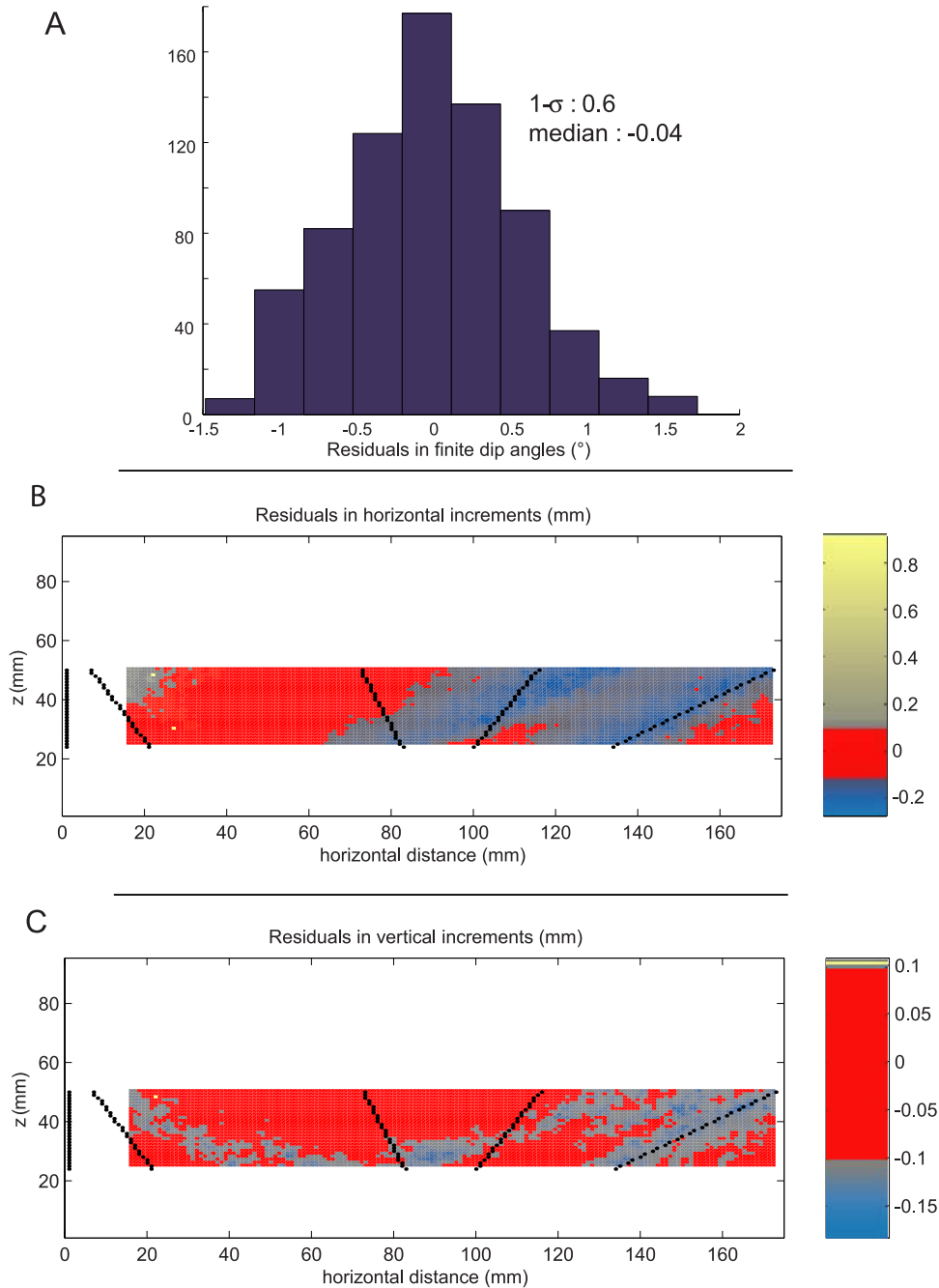


**Figure 21.** Computing the misfits between the observed and the modeled fold kinematics. Residuals correspond to predicted minus observed dips or displacements. (a) Distribution of the computed residuals in the dip angles between predicted and observed finite structures. Standard deviation and median are also reported. The highest residuals are observed in the vicinity of the axial surface lines. (b) Residuals between predicted and observed horizontal incremental displacements for a total incremental displacement of 1 mm at the back of the system. Most of the misfits occur around the shear bands that develop essentially at the front of the fold during steps corresponding to a cumulative shortening of 2.75 mm and 3.4 mm of Figure 18. Except for this area where deformation is underestimated by the model, the predicted horizontal displacements are in good agreement with the observed ones, within 10% of the applied displacement at the back of the system. (c) Residuals between predicted and observed vertical incremental displacements for a total incremental displacement of 1 mm at the back of the system. Most of the underestimation of vertical incremental deformation results also from the influence of the shear bands at the front of the fold. As previously, the model is able to predict correctly the incremental displacements within 10% of the shortening applied at the back of the system.

[42] **Acknowledgments.** We are grateful to Remi Michel for his help in the design of the optical monitoring system. We also thank Jacques Malavieille, Rick Allmendinger, and John Suppe for fruitful discussions. The manuscript has benefited from thorough reviews and helpful suggestions by Hemin Koyi, Jurgen Adam, Mark Fisher, and the Associate Editor Wouter Schellart. The analogue experiments were initiated thanks to a grant by CNRS/INSU to S.D. This study was partly funded by the Gordon and Betty Moore Foundation. This is Caltech Tectonics Observatory contribution 45.

## References

- Adam, J., J. Urai, B. Wieneke, O. Oncken, K. Pfeiffer, N. Kukowski, J. Lohrmann, S. Hoth, W. van der Zee, and J. Schmatz (2005), Shear localisation and strain distribution during tectonic faulting—New insights from granular-flow experiments and high-resolution optical image correlation techniques, *J. Struct. Geol.*, 27(2), 283–301.
- Allmendinger, R. W. (1998), Inverse and forward numerical modeling of trishear fault-propagation folds, *Tectonics*, 17(4), 640–656.
- Allmendinger, R. W., and J. H. Shaw (2000), Estimation of fault propagation distance from fold shape: Implications for earthquake hazard assessment, *Geology*, 28(12), 1099–1102.
- Avouac, J. P., P. Tapponier, M. Bai, H. You, and G. Wang (1993), Active rifting and folding along the northern Tien-Shan and Late Cenozoic rotation of the Tarim relative to Dzungaria and Kazakhstan, *J. Geophys. Res.*, 98(B4), 6755–6804.
- Brooks, B. A., E. Sandvol, and A. Ross (2000), Fold style inversion: Placing probabilistic constraints on the predicted shape of blind thrust faults, *J. Geophys. Res.*, 105(B6), 13,281–13,301.
- Burbank, D., and R. Anderson (2001), *Tectonic Geomorphology*, 274 pp., Blackwell Sci., Malden, Mass.
- Chamberlin, R. T. (1910), The Appalachian folds of central Pennsylvania, *J. Geol.*, 27, 228–251.
- Chapple, W. M. (1978), Mechanics of thin-skinned fold-and-thrust belts, *Geol. Soc. Am. Bull.*, 89(8), 1189–1198.
- Daëron, M., J.-P. Avouac, and J. Charreau (2007), Modeling the shortening history of a fault tip fold using structural and geomorphic records of deformation, *J. Geophys. Res.*, doi:10.1029/2006JB004460, in press.
- Dahlstrom, C. D. A. (1990), Geometric constraints derived from the law of conservation of volume and applied to evolutionary models for detachment folding, *AAPG Bull.*, 74(3), 336–344.
- Davis, D., J. Suppe, and F. A. Dahlen (1983), Mechanics of fold-and-thrust belts and accretionary wedges, *J. Geophys. Res.*, 88(B2), 1153–1172.
- Dominguez, S., J. Malavieille, and S. E. Lallemand (2000), Deformation of margins in response to seamount subduction: Insights from sandbox experiments, *Tectonics*, 19(1), 182–196.
- Dominguez, S., R. Michel, J. P. Avouac, and J. Malavieille (2001), Kinematics of thrust fault propagation, Insight from video processing techniques applied to experimental modeling, paper presented at EGS XXVI, Nice, France, March 2001.
- Dominguez, S., J. Malavieille, and J. P. Avouac (2003), Fluvial terraces deformation induced by thrust faulting: An experimental approach to better estimate crustal shortening velocities, paper presented at EGS-AGU-EUG Joint Assembly, Nice, France.
- Epard, J. L., and R. H. Groshong (1993), Excess area and depth to detachment, *AAPG Bull.*, 77(8), 1291–1302.
- Epard, J. L., and R. H. Groshong (1995), Kinematic model of detachment folding including limb rotation, fixed hinges and layer-parallel strain, *Tectonophysics*, 247(1–4), 85–103.
- Erslev, E. A. (1991), Trishear fault-propagation folding, *Geology*, 19(6), 617–620.
- Gutscher, M. A., N. Kukowski, J. Malavieille, and S. Lallemand (1998), Material transfer in accretionary wedges from analysis of a systematic series of analog experiments, *J. Struct. Geol.*, 20(4), 407–416.
- Hardy, S., and J. Poblet (1994), Geometric and numerical-model of progressive limb rotation in detachment folds, *Geology*, 22(4), 371–374.
- Hardy, S., J. Poblet, K. McClay, and D. Waltham (1996), Mathematical modelling of growth strata associated with fault-related fold structures, *Geol. Soc. Spec. Publ.*, 99, 265–282.
- Horn, B. K. P., and B. G. Schunck (1980), Determining optical flow, *Tech. Rep. A. I. Memo 572*, Mass. Inst. of Technol., Cambridge.
- Jolivet, M. (2000), Cinématique des déformations au Nord Tibet. Thermochronologie, traces de fission, modélisation analogue et études de terrain, thesis, Univ. Montpellier II, Montpellier, France.
- King, G. C. P., R. S. Stein, and J. B. Rundle (1988), The growth of geological structures by repeated earthquakes. 1. Conceptual-framework, *J. Geophys. Res.*, 93(B11), 13,307–13,318.
- Konstantinovskaia, E., and J. Malavieille (2005), Erosion and exhumation in accretionary orogens: Experimental and geological approaches, *Geochim. Geophys. Geosyst.*, 6, Q02006, doi:10.1029/2004GC000794.
- Koyi, H. (1995), Mode of internal deformation in sand wedges, *J. Struct. Geol.*, 17(2), 293–300.
- Koyi, H. A., and J. Cotton (2004), Experimental insights on the geometry and kinematics of fold-and-thrust belts above weak, viscous evaporitic decollement; a discussion, *J. Struct. Geol.*, 26(11), 2139–2141.
- Koyi, H., and B. Maillot (2006), The effect of ramp dip and friction on thickness change of hangingwall units: A necessary improvement to kinematic models, paper presented at the annual general meeting of the Tectonic Studies Group of the Geological Society of London, Manchester, U.K.
- Krantz, R. W. (1991), Measurements of friction coefficients and cohesion for faulting and fault reactivation in laboratory models using sand and sand mixtures, *Tectonophysics*, 188(1–2), 203–207.
- Lallemand, S. E., P. Schnurle, and J. Malavieille (1994), Coulomb theory applied to accretionary and nanoaccretionary wedges: Possible causes for tectonic erosion and or frontal accretion, *J. Geophys. Res.*, 99(B6), 12,033–12,055.
- Lavé, J., and J. P. Avouac (2000), Active folding of fluvial terraces across the Siwaliks Hills, Himalayas of central Nepal, *J. Geophys. Res.*, 105(B3), 5735–5770.
- Lohrmann, J., N. Kukowski, J. Adam, and O. Oncken (2003), The impact of analogue material properties on the geometry, kinematics, and dynamics of convergent sand wedges, *J. Struct. Geol.*, 25(10), 1691–1711.
- Maillot, B., and H. Koyi (2006), Thrust dip and thrust refraction in fault-bend folds: Analogue models and theoretical predictions, *J. Struct. Geol.*, 28(1), 36–49.
- Maillot, B., and Y. M. Leroy (2003), Optimal dip based on dissipation of backthrusts and hinges in fold-and-thrust belts, *J. Geophys. Res.*, 108(B6), 2320, doi:10.1029/2002JB002199.
- Malavieille, J. (1984), Modélisation expérimentale des chevauchements imbriqués: Application aux chaînes de montagnes, *Bull. Soc. Geol. Fr.*, XXVI(1), 129–138.
- Marone, C. (1998), Laboratory-derived friction laws and their application to seismic faulting, *Annu. Rev. Earth Planet. Sci.*, 26, 643–696.
- Medwedeff, D. A., and J. Suppe (1997), Multibend fault-bend folding, *J. Struct. Geol.*, 19(3–4), 279–292.
- Mitra, S. (2003), A unified kinematic model for the evolution of detachment folds, *J. Struct. Geol.*, 25(10), 1659–1673.
- Molnar, P., et al. (1994), Quaternary climate-change and the formation of river terraces across growing anticlines on the north flank of the Tien-Shan, China, *J. Geol.*, 102(5), 583–602.
- Mosar, J., and J. Suppe (1992), Role of shear in fault-propagation folding, in *Thrust Tectonics*, edited by K. R. McClay, pp. 123–132, CRC Press, Boca Raton, Fla.
- Mulugeta, G. (1988), Squeeze box in a centrifuge, *Tectonophysics*, 148(3–4), 323–335.
- Mulugeta, G., and H. Koyi (1992), Episodic accretion and strain partitioning in a model sand wedge, *Tectonophysics*, 202(2–4), 319–333.
- Myers, W. B., and W. Hamilton (1964), Deformation accompanying the Hebgen Lake earthquake of August 17, 1959, in *The Hebgen Lake, Montana, Earthquake of August 17, 1959*, U.S. Geol. Surv. Prof. Pap., 435, 55–98.
- Okada, Y. (1985), Surface deformation due to shear and tensile faults in a half-space, *Bull. Seismol. Soc. Am.*, 75(4), 1135–1154.
- Poblet, J., and K. McClay (1996), Geometry and kinematics of single-layer detachment folds, *AAPG Bull.*, 80(7), 1085–1109.
- Press, W. H., S. A. Teukolsky, W. T. Vetterling, and B. P. Flannery (1995), *Numerical Recipes in C: The Art of Scientific Computing*, Cambridge Univ. Press, New York.
- Rockwell, T. K., E. A. Keller, and G. R. Dembroff (1988), Quaternary rate of folding of the Ventura Avenue anticline, Western Transverse Ranges, southern California, *Geol. Soc. Am. Bull.*, 100(6), 850–858.
- Savage, H. M., and M. L. Cooke (2004), The effect of non-parallel thrust fault interaction on fold patterns, *J. Struct. Geol.*, 26(5), 905–917.
- Scharer, K. M., D. W. Burbank, J. Chen, R. J. Weldon, C. Rubin, R. Zhao, and J. Shen (2004), Detachment folding in the southwestern Tian Shan-Tarim foreland, China: Shortening estimates and rates, *J. Struct. Geol.*, 26(11), 2119–2137.
- Schellart, W. P. (2000), Shear test results for cohesion and friction coefficients for different granular materials: Scaling implications for their usage in analogue modelling, *Tectonophysics*, 324(1–2), 1–16.
- Simoes, M., J. P. Avouac, and Y.-G. Chen (2007a), Slip rates on the Chelungpu and Chushiang thrust faults inferred from a deformed strath terrace along the Dzunguna river, west central Taiwan, *J. Geophys. Res.*, doi:10.1029/2005JB004200, in press.
- Simoes, M., J.-P. Avouac, Y.-G. Chen, A. K. Singhvi, C.-Y. Wang, M. Jaiswal, Y.-C. Chan, and S. Bernard (2007b), Kinematic analysis of the Pakuashan fault tip fold, west central Taiwan: Shortening rate and age of folding inception, *J. Geophys. Res.*, doi:10.1029/2005JB004198, in press.



- Stein, R. S., G. C. P. King, and J. B. Rundle (1988), The growth of geological structures by repeated earthquakes: 2. Field examples of continental dip-slip faults, *J. Geophys. Res.*, *93*(B11), 13,319–13,331.
- Storti, F., and J. Poblet (1997), Growth stratal architectures associated to décollement folds and fault-propagation folds: Inferences on fold kinematics, *Tectonophysics*, *282*(1–4), 353–373.
- Suppe, J. (1983), Geometry and kinematics of fault-bend folding, *Am. J. Sci.*, *283*(7), 684–721.
- Suppe, J., and D. A. Medwedeff (1990), Geometry and kinematics of fault-propagation folding, *Eclogae Geol. Helv.*, *83*(3), 409–454.
- Suppe, J., G. T. Chou, and S. C. Hook (1992), Rates of folding and faulting determined from growth strata, in *Thrust Tectonics*, edited by K. R. McClay, pp. 105–121, CRC Press, Boca Raton, Fla.
- Thompson, S. C., R. J. Weldon, C. M. Rubin, K. Abdrakhmatov, P. Molnar, and G. W. Berger (2002), Late Quaternary slip rates across the central Tien Shan, Kyrgyzstan, central Asia, *J. Geophys. Res.*, *107*(B9), 2203, doi:10.1029/2001JB000596.
- Van der Woerd, J., X. W. Xu, H. B. Li, P. Tapponnier, B. Meyer, F. J. Ryerson, A. S. Meriaux, and Z. Q. Xu (2001), Rapid active thrusting along the northwestern range front of the Tanghe Nan Shan (western Gansu, China), *J. Geophys. Res.*, *106*(B12), 30,475–30,504.
- Ward, S. N., and G. Valensise (1994), The paleo-verdes terraces, California: Bathtub rings from a buried reverse fault, *J. Geophys. Res.*, *99*(B3), 4485–4494.
- Whitaker, A. E., and M. J. Bartholomew (1999), Layer parallel shortening: A mechanism for determining deformation timing at the junction of the central and southern Appalachians, *Am. J. Sci.*, *299*(3), 238–254.
- Wickham, J. (1995), Fault displacement-gradient folds and the structure at Lost Hills, California (USA), *J. Struct. Geol.*, *17*(9), 1293–1302.
- Zehnder, A. T., and R. W. Allmendinger (2000), Velocity field for the Trishear model, *J. Struct. Geol.*, *22*(8), 1009–1014.

---

J.-P. Avouac, Tectonics Observatory, California Institute of Technology, Division of Geological and Planetary Sciences, Mail Code 100-23, Pasadena, CA 91125, USA.

S. Bernard, Laboratoire de Géologie, UMR 8538, CNRS, Ecole Normale Supérieure 24 rue Lhomond, F-75231 Paris Cedex 05, France. (sylvain.bernard@ens.fr)

S. Dominguez, Laboratoire Dynamique de la Lithosphère, UMR CNRS/UMII 5573 - Bât. 22 (cc. 60), Place Bataillon, F-34095 Montpellier Cedex 5, France.

M. Simoes, Equipe “Bassins Sédimentaires” - UMR 6118, Géosciences Rennes- CNRS/Université Rennes 1, Campus de Beaulieu, F-35042 Rennes Cedex, France.